Journal of Asian Earth Sciences 180 (2019) 103849

Contents lists available at ScienceDirect

Journal of Asian Earth Sciences

journal homepage: www.elsevier.com/locate/jseaes

Full length article

Heterogeneous lithospheric mantle beneath the southeastern Tibetan Plateau: Evidence from Cenozoic high-Mg potassic volcanic rocks in the Jinshajiang–Ailaoshan Cenozoic magmatic belt

Yue Xu[a,b,c], Jingjing Zhu[c], Ruizhong Hu[d], Xianwu Bi[c,*], Hongjun Yu[a], Leiluo Xu[c], Baohua Liu[a], Mingliang Huang[c], Xiangyuan Sheng[c]

[a] National Deep Sea Center, State Ocean Administration, Qingdao 266237, China
[b] Ocean University of China, Qingdao 266100, China
[c] State Key Laboratory of Ore Deposit Geochemistry, Institute of Geochemistry, Chinese Academy of Sciences, Guiyang 550081, China
[d] School of Earth and Planetary Sciences, University of Chinese Academy of Sciences, Beijing 100049, China

ARTICLE INFO

Keywords:
High-Mg potassic volcanic rocks
Sr-Nd-Pb-Hf isotope
Heterogeneous lithospheric mantle
Metasomatism
Jinshajiang–Ailaoshan
Tibetan Plateau

ABSTRACT

Cenozoic (~40–30 Ma) high-Mg potassic volcanic rocks are abundant in the Jinshajiang–Ailaoshan magmatic belt that stretches from eastern Tibet to western Yunnan. The petrogenesis and compositional variation of the mantle source of these rocks are poorly known. In this paper, we obtained U-Pb zircon ages and whole-rock major and trace element and Sr-Nd-Pb-Hf isotopic data for these volcanic rocks from the Nangqian basin in the Eastern Qiangtang block, eastern Tibet. High-Mg volcanic rocks in Nangqian are potassic trachybasalts, shoshonites and latites and contain 6.49–10.54 wt% MgO, 48.04–56.89 wt% SiO_2 and 3.36–4.14 wt% K_2O, with K_2O/Na_2O ratios of 0.94–1.24. Zircon U-Pb dating shows that they are slightly older (40–38 Ma) than their counterparts (37–32 Ma) from the Dali district, western Yunnan. They are enriched in large ion lithophile elements (LILEs) and light rare earth elements (LREEs) and have significantly negative Nb-Ta-Ti anomalies. Isotopically, they have primitive mantle-like $^{87}Sr/^{86}Sr$ ratios (0.7050–0.7055) and εNd(t) values of −1.06 to +0.10 and restricted ranges of $^{206}Pb/^{204}Pb$ (18.63–18.71), $^{207}Pb/^{204}Pb$ (15.52–15.57) and $^{208}Pb/^{204}Pb$ ratios (38.42–38.59). Zircon εHf(t) values vary from +4.1 to +9.4 and are thus decoupled from their whole-rock Nd isotope ratios. Previous studies have shown that Cenozoic high-Mg potassic volcanic rocks in the Dali district have more enriched Sr-Nd-Pb-Hf isotopic compositions, higher LILE/HFSE (high field strength elements) and LILE/LREE ratios but less enrichment in LREE than the counterparts from the Nangqian basin. Geochemical differences between high-Mg volcanic rocks from these two locations can be explained by different mantle sources caused by different metasomatic processes. Underneath the Nangqian basin, a juvenile, isotopically "depleted", and garnet-bearing lithospheric mantle was metasomatized by Paleozoic and Cenozoic subduction, whereas an ancient (probably as old as Neoproterozoic), fertilized, and spinel facies-dominated lithospheric mantle was metasomatized by Neoproterozoic subduction underneath the Dali district.

1. Introduction

The Tibetan plateau was uplifted in association with the continued Indian-Euroasian convergence that was initiated in the Eocene (~62–58 Ma) (Wang et al., 2018a, 2015; Hu et al., 2017, 2016; Deng et al., 2014b; Hou et al., 2003). However, questions concerning the post-collisional tectonic evolution, the nature of the mantle source, and metasomatic processes are unresolved (Sun et al., 2018; Wang et al., 2018a; Wang et al., 2016; Liu et al., 2016, 2015; Deng et al., 2014a, b; Wang et al., 2008). Answers may be found in the variation of the major and trace element and isotope geochemistry of high-Mg potassic magmas.

High-Mg potassic magmas are almost exclusively produced in intra-continental and post-collisional settings (Prelević et al., 2012; Chung et al., 2005; Foley et al., 1987). They are generally characterized by enrichments in K (both absolute and relative to Na) and incompatible trace elements, and can be collectively used to probe the lithospheric mantle and explore metasomatic processes (Pang et al., 2015; Prelević et al., 2012, 2008; Conticelli et al., 2009; Foley et al., 1987). Cenozoic high-Mg potassic igneous rocks postdate the Indian-Euroasian

* Corresponding author.
E-mail address: bixianwu@vip.gyig.ac.cn (X. Bi).

https://doi.org/10.1016/j.jseaes.2019.04.018
Received 6 December 2018; Received in revised form 29 April 2019; Accepted 29 April 2019
Available online 03 May 2019
1367-9120/

continental collision and are widespread in the southern parts of the Tibetan Plateau and adjacent regions to the east (e.g. Xu et al., 2017; Lu et al., 2015; Huang et al., 2010; Guo et al., 2005). They have been used to investigate the composition of the mantle sources and the geodynamic processes in a post-collisional environment at different locations from Tibet to Yunnan (Fu et al., 2018; Liu et al., 2015; Lu et al., 2015; Huang et al., 2010; Zhao et al., 2009; Mo et al., 2006; Guo et al., 2006, 2005; Chung et al., 2005, 1998; Ding et al., 2003; Xu et al., 2001; Miller et al., 1999; Turner et al., 1996).

The Jinshajiang and Ailaoshan sutures in the Sanjiang Tethyan Orogen are marked by remnants of oceanic lithosphere of the Paleo-Tethys Ocean branches (Wang et al., 2018b; Deng et al., 2014b; Mo et al, 1993). Eocene to Oligocene (~40–30 Ma) magmatism formed the prominent Jinshajiang–Ailaoshan (JSAS) magmatic belt that stretches from eastern Tibet to western Yunnan for ~2000 km (Hou et al., 2007; Chung et al., 1998). It consists of potassic mafic volcanic and felsic intrusive rocks and contains numerous porphyry-skarn Cu-Au and polymetallic deposits (Xu et al., 2012; Deng et al., 2014a, b; Lu et al., 2013a, b, 2012; Hou et al., 2003). High-Mg potassic volcanic rocks (> 6 wt% MgO) in this belt are most abundant in two areas: the Nangqian basin of the Eastern Qiangtang block, SE Tibet, and the Dali district in the western margin of the Yangtze block (Fig. 1; Huang et al., 2010; Guo et al., 2005; Spurlin et al., 2005; Sun et al., 2001; Xu et al., 2001; Chung et al., 1998).

In the Nangqian basin, felsic intrusions show geochemical signatures of a subduction origin; they are coeval to the Paleocene–Eocene NE–SW shortening that was induced by continental subduction (Xu et al., 2016; Spurlin et al., 2005; Horton et al., 2002). The nature of the underlying mantle is unclear, because previous studies used mostly low MgO rocks (< 6 wt%). Unlike their high-Mg associates, these low MgO potassic rocks may have experienced higher degrees of crustal contamination during fractional crystallization, obscuring constraints on the nature of mantle source (Xu et al., 2017; Guo et al., 2015; Liu et al., 2015; Huang et al., 2010). The origin of the high-Mg potassic rocks in the Dali district has been a matter of debate for a long time, since models include the occurrence of an exotic Tibetan lithospheric component in the mantle source (Xu et al., 2001), carbonatitic melt metasomatism arising from the seismic low-velocity zone (LVZ) (Huang et al., 2010), and also a metasomatized mantle modified by slab-derived fluids associated with ancient (i.e., prior to Cenozoic) subduction events (Lu et al., 2015; 2013b; Yang et al., 2015; Guo et al., 2005; Bi et al., 2004; Deng et al., 1998; Zhang and Xie, 1997).

In this study, we present new whole-rock elemental and Sr-Nd-Pb isotopic compositions and in-situ U-Pb ages and Hf isotopes of zircon grains from high-Mg volcanic rocks in the Nangqian basin. We compare the Cenozoic high-Mg volcanic rocks from this basin and with those of the Dali district based on available geochemical data (Huang et al., 2010; Guo et al., 2005; Xu et al., 2001) and draw conclusions on the nature of the sub-continental lithospheric mantle (SCLM) beneath the Jinshajiang–Ailaoshan suture. We discuss the origin of the mantle sources underneath these two areas and propose a model where different processes are responsible for the differences in their mantle sources.

2. Geological background

2.1. Tectonic framework of eastern Tibet and western Yunnan

The collision of arc terranes and micro-continental blocks formed the eastern Tibetan Plateau (Fig. 1; Deng et al., 2014a; Metcalfe, 2013, and references therein). From north to south, there are four micro-continental blocks, namely the Songpan–Ganze, Eastern Qiangtang, Western Qiangtang, and Lhasa blocks. They are separated by the Paleo-Tethyan Jinshajiang, the paleo-Thetyan Longmu Tso–Shuanghu, and the Meso-Tethyan Bangonghu–Nujiang sutures, respectively. All of these blocks were amalgamated before the Cenozoic to form the southern part of the Eurasian supercontinent (Fig. 1; Deng et al., 2014a; Metcalfe, 2013; Zhu et al., 2013). The Jinshajiang Paleo-Tethys Ocean was gradually consumed by a prolonged westward subduction from Devonian to Triassic, recorded by the S–N-trending Jiangda–Weixi arc belt (Wang et al., 2018b; Deng et al., 2014a; Metcalfe, 2013; Mo et al., 1993). It is inferred that the mantle beneath the Eastern Qiangtang block could have been modified by slab-derived fluids or melts generated during the Paleo-Tethyan oceanic subduction events.

To the east are three Gondwana-derived micro-continental blocks: the West Burma (or Tengchong) block, the Sibumasu (or Baoshan) block and the Indochina (or Simao) block from west to east. They were amalgamated with the South China block before the Cenozoic, forming the southeastern part of the Eurasian supercontinent (Fig. 1; Deng et al., 2014a; Metcalfe, 2013). The Ailaoshan suture separates the Simao and South China blocks and marks the closure of the Ailaoshan Paleo-Tethys branch at Late Triassic (Wang et al., 2018b; Deng et al., 2014a, 2014b). In the Dali district of the western margin of the South China block, ~850–740 Ma mafic and felsic rocks define an active continental margin environment, associated with the Neoproterozoic circum-Rodinia subduction system (Zhou et al., 2014, 2006, and references therein).

Based on the observation that Late Paleozoic arc basalts are present only on the western side of the suture, a westward subduction polarity has been proposed (Fan et al., 2010; Jian et al., 2009). Thus, the western rim of the South China block was a passive continental margin during the Paleozoic, although more accurate paleogeographic reconstruction is needed. It was an active continental margin in the Neoproterozoic, as indicated by protracted subduction-related magmatism in the region (Zhou et al., 2006).

2.2. The Eocene–Oligocene JSAS magmatic belt

Eocene–Oligocene (~40–30 Ma) potassic igneous rocks are widespread in eastern Tibet and western Yunnan and are associated with shearing and granulite metamorphism (Liu et al., 2017; Yang et al., 2019a, 2019b and references therein). These rocks include trachybasalts, shoshonites, olivine latites, and trachytes (Huang et al., 2010; Guo et al., 2005; Wang et al., 2001; Chung et al., 1998). They were formed after the Indian-Euroasian continental collision as early as 62–58 Ma (Zheng and Wu, 2018; Ding et al., 2017, 2016; Hu et al., 2017; Zhu et al., 2017;Wu et al., 2014). A post-collisional setting is invoked for these rocks (e.g. Liu et al., 2015; Zhao et al., 2009; Chung et al., 2005). The JSAS magmatic belt is spatially associated with the Cenozoic JSAS fault systems (e.g., Chung et al., 2005, 1998; Xia et al., 2011). From eastern Tibet to western Yunnan, three major potassic volcanic clusters, the Nangqian, Mangkang, and Dali clusters, are present in the belt (Fig. 1; Chung et al., 1998). There are high-Mg volcanic rocks in the Mangkang area, although the are relatively sparse (Zhang et al., 2005; Chung et al., 1998).

The Nangqian basin in the northern margin of the Eastern Qiangtang block (Fig. 1; Hou et al., 2003) is bounded by the Late Paleozoic Zuogong–Jinghong volcanic arc to the southwest and by the Late Paleozoic Jiangda–Weixi volcanic arc to the northeast (Zi et al., 2013; Liu et al., 1993). Field mapping, and sedimentological–structural data from the Yushu–Nangqian thrust belt support a protracted deformation history and Cenozoic NE–SW shortening associated with a continental subduction (Spurlin et al., 2005; Horton et al., 2002). Basaltic trachyandesites and trachydacites (MgO < 6 wt%) in the Nanqgian basin have ages of ~38 Ma, and are interbedded with Paleocene–Late Eocene sedimentary rocks (Horton et al., 2002).

3. Sample description

High-Mg volcanic rocks from the Boza area in the Nangqian basin (Fig. 2) include potassic trachybasalt, shoshonite, and latite (Table 1). They are relatively fresh, and have a porphyritic texture (Fig. 3).

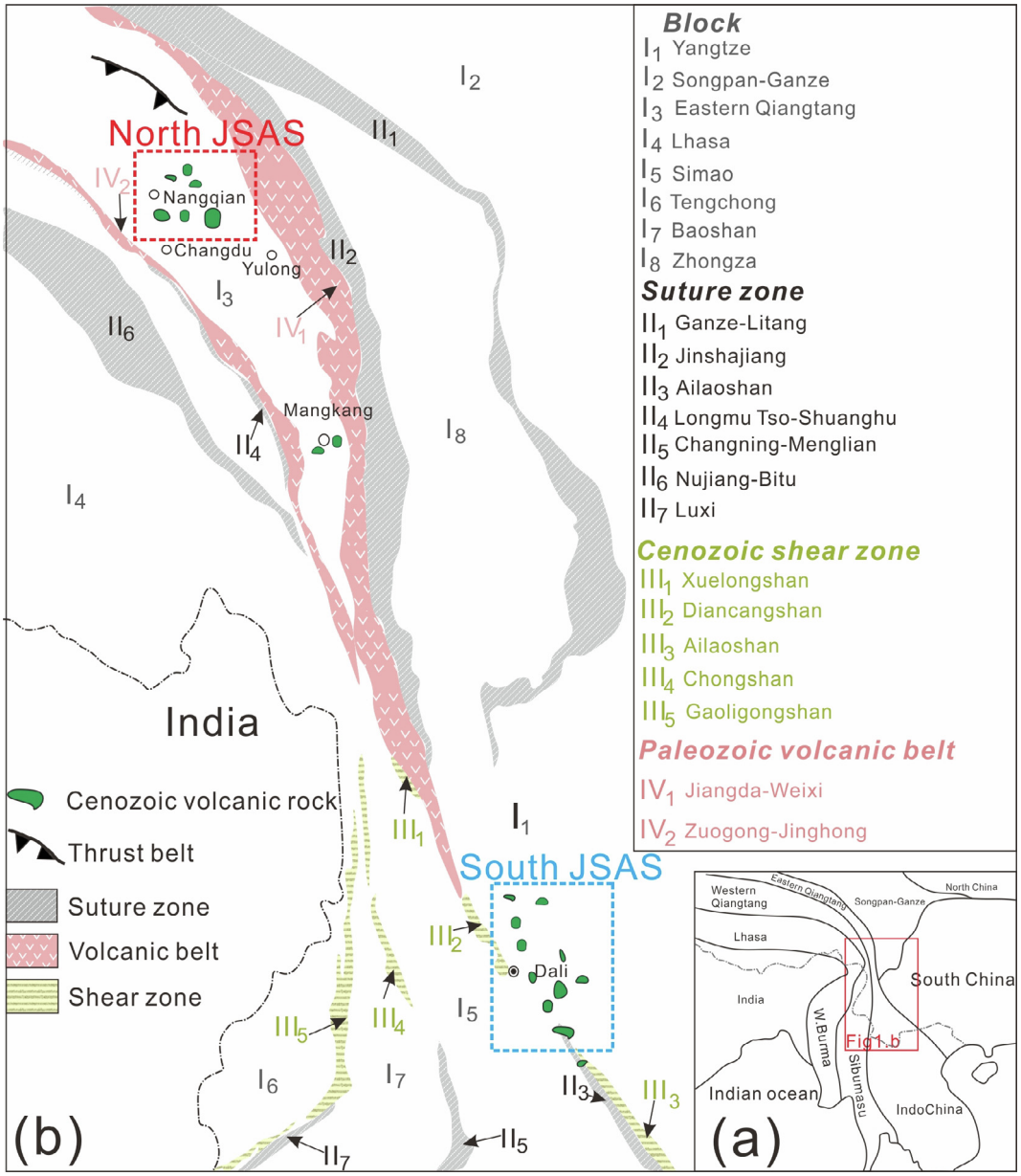

Fig. 1. (a) The distribution of principal continental blocks and sutures of Southeast Asia (modified after Metcalfe, 2013); (b) Simplified geological map of the Eastern Tibetan plateau and surrounding areas (modified from Deng et al., 2014a) showing tectonic framework and distributions of Cenozoic volcanic rocks in the JSAS magmatic belt.

Potassic trachybasalts from interbedded volcanic flows contain phenocrysts (3–12 vol%) of orthopyroxene (0.1–0.8 mm), clinopyroxene (0.1–0.5 mm), and phlogopite (0.1–0.3 mm). Minerals in the hyalopilitic groundmass are composed mainly of microlitic clinopyroxene, phlogopite, sanidine, apatite, zircon and magnetite (Fig. 3a, b and g; Table 1).

Shoshonites and latites from Paleocene–Late Eocene volcanic flows occur as small stocks and dikes. They contain phenocrysts of clinopyroxene, sanidine, phlogopite, and minor orthopyroxene (Fig. 3c–f and h–i; Table 1). Minerals in the groundmass are mainly clinopyroxene, sanidine, phlogopite, and orthopyroxene. Accessory minerals include apatite, zircon, and magnetite (Fig. 3f and h). Some latite rocks show typical glomeroporphyritic texture, such as clinopyroxene aggregation (Fig. 3i).

4. Analytical methods

4.1. Zircon LA-ICP-MS U-Pb dating

Samples BZ05-1, BZ04-2, and BZ03-3 were used for zircon separation. About 50 kg of each sample were crushed and then zircon grains separated using standard density and magnetic separation techniques. Representative grains were handpicked, mounted on an epoxy resin disk, and polished. The internal structure was examined using cathodoluminescence (CL) microscopy prior to U-Pb isotopic analyses. The CL imaging was carried out using a JSM-7088F scanning electron microscope equipped with a Gatan MONO CL4 detector at the State Key Laboratory of Ore Deposit Geochemistry, Institute of Geochemistry, Chinese Academy of Sciences (SKLODG).

Zircon U-Pb analyses were performed using a laser ablation inductively coupled plasma mass spectrometer (LA-ICP-MS) at the State Key Laboratory of Geological Processes and Mineral Resources, China

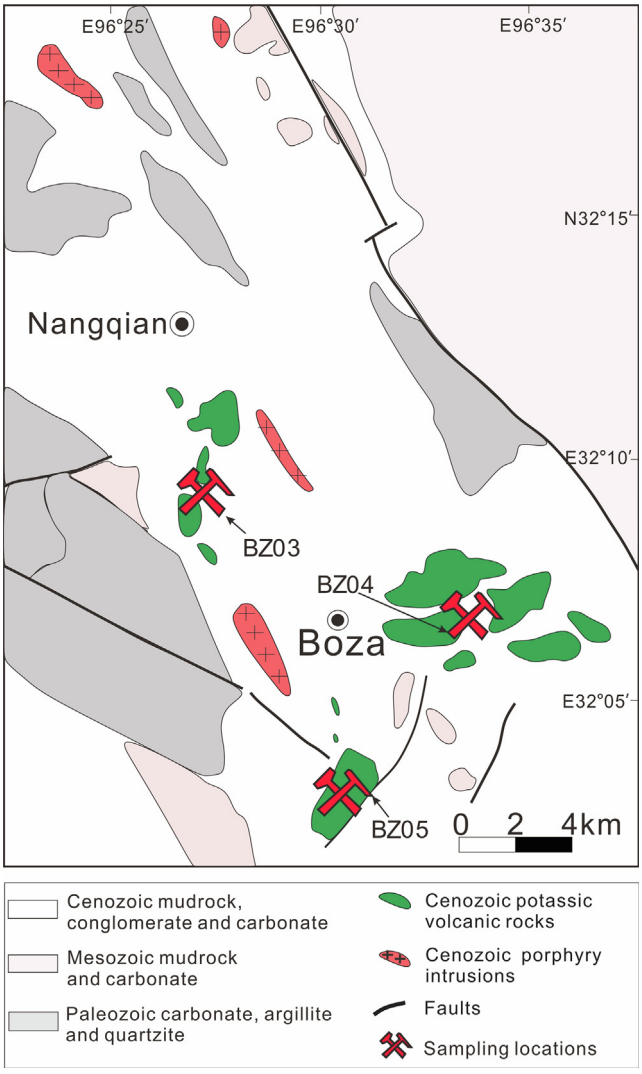

Fig. 2. Simplified geological map of the Nangqian basin, illustrating distribution of Eocene potassic volcanic rocks and sample locations (modified after Xu et al., 2016; Deng et al., 2000).

University of Geosciences, Wuhan, China. A pulsed (Geolas) 193-nm ArF Excimer (Lambda Physik, Göttingen Germany) laser with 50 mJ/pulse energy was used for ablation at a repetition rate of 10 Hz. The diameter of the laser beam was 32 μm. The detailed analytical procedures were described by Liu et al. (2010, 2008). Helium was the carrier gas and Argon as the makeup gas was mixed with the carrier gas via a T-connector before entering the ICP. Harvard zircon 91500 was used as an external standard to normalize isotopic fractionation during analyses. The NIST 610 glass was the external standard to calculate U, Th, and Pb concentrations of the unknowns. Ion signal intensities were acquired with an Agilent 7500a ICP-MS instrument. Each analyses incorporated a background acquisition of approximately 20–30 s (gas blank) followed by 50 s of data acquisition from the sample. Off-line selection and integration of background and analyte signals, and time drift correction and quantitative calibration for U-Pb dating were performed with the ICPMSDatacal program (Liu et al., 2010, 2008). A common Pb correction was applied using the method of Anderson (2002), which has only a minimal effect on the age results. Concordia diagrams, and intercepted age and weighted mean age calculations were carried out using the Isoplot/Ex (version 4.15) of Ludwig (2012).

4.2. Whole-rock major and trace element analyses

Rocks were crushed to a roughly 200-mesh powder in a corundum mill. Fused lithium tetraborate glass pellets were analyzed with a PANalytical Axios-advance X-ray fluorescence spectrometer (XRF) at the SKLODG, to obtain whole-rock major elements. Loss on ignition (LOI) was obtained using 1 g of powder heated to 1100 °C for one hour. Analytical precision as determined with the Chinese National standard GSR-1 was generally better than 5%. Trace elements were analysed from solution with a PE DRC-e ICP-MS at the SKLODG. Powdered samples (50 mg) were dissolved in PTFE-lined stainless steel bombs using a HF + HNO_3 mixture for 48 h at ~190 °C. Rh was the internal standard to monitor signal drift during counting. The international standards GSR-1, JG-2, G-2, NIM-G, SG-3, and SG-1a were used for monitoring analytical quality. The analytical uncertainty was generally better than 5%. Detailed analytical methods are described in Qi et al. (2000).

4.3. Whole-rock Sr-Nd isotopic analyses

Whole-rock Sr-Nd isotope compositions were analyzed at the

Table 1
Phenocryst and groundmass mineralogy of high-Mg volcanic rocks from Boza area in the Nangqian basin.

Sample no.	Lithology	Texture	Phenocrysts	Groundmass
Boza, the Nangqian basin				
BZ04-5-1	Potassic trachybasalt	porphyritic	Opx(2), Cpx(2)	Cpx, Phl, Sa, Ap, Mag
BZ05-1	Potassic trachybasalt	porphyritic	Opx(12), Cpx(6)	Cpx, Phl, Sa, Zrn, Mag
BZ05-2	Potassic trachybasalt	porphyritic	Opx(3), Cpx(2),Phl(1)	Cpx, Phl, Sa, Mag
BZ05-3	Potassic trachybasalt	porphyritic	Opx(2), Cpx(1), Phl(1)	Cpx, Phl, Sa, Mag
BZ05-4	Potassic trachybasalt	porphyritic	Opx(4), Cpx(3)	Cpx, Phl, Sa, Mag
BZ05-5	Potassic trachybasalt	porphyritic	Opx(8), Cpx(4)	Cpx, Phl, Sa, Zrn, Mag
BZ05-6	Potassic trachybasalt	porphyritic	Opx(3), Cpx(2)	Cpx, Phl, Sa, Mag
BZ05-7	Potassic trachybasalt	porphyritic	Opx(7), Cpx(3), Phl(1)	Cpx, Phl, Sa, Zrn, Mag
BZ04-2	Shoshonite	porphyritic	Opx(3), Cpx(10), Sa (1)	Cpx, Sa, Zrn, Mag
BZ04-3	Shoshonite	porphyritic	Opx(1), Cpx(3) , Phl(1)	Cpx, Sa, Ap, Mag
BZ04-5	Latite	porphyritic	Opx(2), Cpx(4), Sa (1)	Cpx, Phl, Sa, Ap, Mag
BZ04-6	Shoshonite	porphyritic	Opx(3), Cpx(2), Sa (2), Phl(1)	Cpx, Phl, Sa, Ap, Mag
BZ04-7	Latite	porphyritic	Opx(3), Cpx(6), Phl(1)	Cpx, Sa, Mag
BZ03-3	Latite	porphyritic	Opx(2), Cpx(12), Sa(3), Phl (1)	Cpx, Sa, Ap, Zrn, Mag
BZ03-4	Latite	porphyritic	Opx(1), Cpx(9), Sa(3)	Cpx, Sa, Ap, Mag
BZ03-5	Latite	porphyritic	Cpx(2), Sa(1)	Cpx, Sa, Ap, Mag
BZ03-6	Latite	porphyritic	Cpx(8), Sa(3), Phl (1)	Cpx, Sa, Zrn, Mag
BZ03-7	Latite	porphyritic	Opx(2), Cpx(7)	Cpx, Sa, Mag

Abbreviations: Ap = apatite; Cpx = clinopyroxene; Mag = magnetite; Opx = orthopyroxene; Phl = phlogopite; Sa = sanidine; Zrn = zircon. Proportions in percent of phenocrysts shown in parentheses (vol. %).

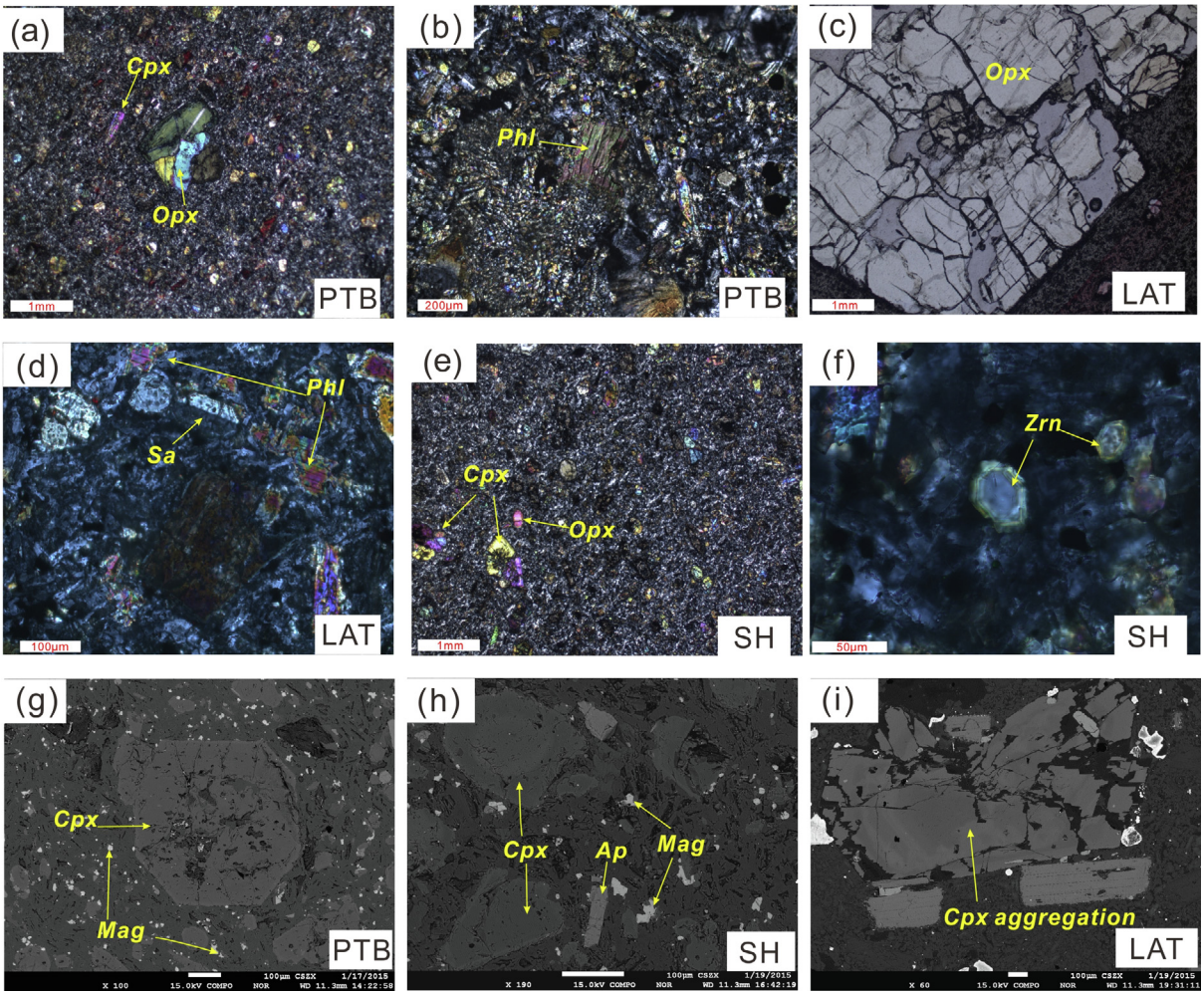

Fig. 3. Photomicrographs (a–f) and back-scattered electron images (g–i) of high-Mg volcanic rocks from the Boza area in the Nangqian basin. Abbreviations: Ap = apatite; Cpx = clinopyroxene; LAT = latite; Mag = magnetite; Opx = orthopyroxene; Phl = phlogopite; PTB = potassic trachybasalt; Sa = sanidine; SH = shoshonite; Zrn = zircon.

SKLODG. Powdered samples were spiked with mixed isotope tracers and dissolved in Teflon capsules with HF + HNO_3. Strontium and REE fractions were separated in solution using cationic ion-exchange resin columns. Then, Nd was separated from the REE fraction using cationic ion-exchange columns and P507 extraction and eluviation resin (Zhang et al., 2002; Richard et al., 1976). The collected Sr and Nd fractions were evaporated and analyzed by a TRITON Thermal Ionization Mass Spectrometer (TIMS) at SKLODG. The mass fractionation correction for Sr and Nd isotopic ratios are based on a $^{86}Sr/^{88}Sr$ of 0.1194 and $^{146}Nd/^{144}Nd$ of 0.72419, respectively. Reference standards NBS987 for Sr and La Jolla for Nd used during whole-rock Sr-Nd isotope analyses resulted in a $^{87}Sr/^{86}Sr$ of 0.710255 ± 0.000006 (2σ, n = 100) and a $^{143}Nd/^{144}Nd$ of 0.512096 ± 0.000004 (2σ, n = 100), respectively. $^{87}Rb/^{86}Sr$ and $^{147}Sm/^{144}Nd$ were calculated using whole-rock Rb, Sr, Sm and Nd values in Table 3. The present day Chondritic Uniform Reservoir (CHUR) values [$(^{87}Rb/^{86}Sr)_{CHUaluR}$ = 0.0847 (McCulloch and Black, 1984); $(^{87}Sr/^{86}Sr)_{CHUR}$ = 0.7045 (DePaolo, 2012); $(^{147}Sm/^{144}Nd)_{CHUR}$ = 0.1967 (Jacobsen and Wasserburg, 1980); $(^{143}Nd/^{144}Nd)_{CHUR}$ = 0.512638 (Goldstein et al., 1984)] were used for the calculations. Nd depleted mantle model ages (T_{DM}) were calculated using $(^{147}Sm/^{144}Nd)_{DM}$ = 0.2137 and $(^{143}Nd/^{144}Nd)_{DM}$ = 0.51315 (Peucat et al., 1989) at the present day. $\lambda_{Rb} = 1.42 \times 10^{-11}$ a^{-1} (Steiger and Jäger, 1977); $\lambda_{Sm} = 6.54 \times 10^{-12}$ a^{-1} (Lugmair and Marti, 1978). Initial $^{87}Sr/^{86}Sr$ ratios and εNd (t) values are corrected using zircon U-Pb ages.

4.4. Whole-rock Pb isotopic analyses

Two-hundred mg sample powders were spiked and dissolved in concentrated HF at 800 °C for 72 h in a Teflon cup. Lead was separated and purified using conventional anion-exchange techniques with dilute HBr as eluent (Zhang et al., 2002). The whole procedural blank was less than 0.4 ng Pb. Lead isotopic ratios were measured with a Finnigan MAT-261 Thermal Ionization Mass Spectrometer (TIMS) at the Laboratory of Radiogenic Isotope Geochemistry, Wuhan Institute of Geology and Mineral Resources, China. During the analyses, the international standard NBS981 yielded a weighted mean $^{206}Pb/^{204}Pb$ of 16.938 ± 0.011 (2σ, n = 30) (the recommended value is 16.9356), a $^{207}Pb/^{204}Pb$ of 15.493 ± 0.012 (2σ, n = 30) (the recommended value is 15.4891), and a $^{208}Pb/^{204}Pb$ of 36.710 ± 0.027 (2σ, n = 30) (the recommended value is 36.7006) (Todt et al., 1996).

4.5. Zircon Hf isotopic analyses

In-situ zircon Hf isotopic compositions were measured using a Neptune multi-collector ICP-MS equipped with a New Wave 193-nm FX laser ablation system (LA-MC-ICP-MS) at the Laboratory of Geoanalysis and Geochronology, Tianjin Institute of Geology and Mineral Resources. Based on the CL images of the zircons, Hf analyses spots for zircons were selected near the previous LA-ICP-MS U-Pb dating spots, so that they were located in a common magmatic oscillatory zone.

Table 2
Zircon U-Pb isotopic data obtained by LA-ICPMS of high-Mg volcanic rocks from Boza area in the Nangqian basin.

Spot	Th(ppm)	U(ppm)	Th/U	$^{238}U/^{206}Pb$	1σ	$^{207}Pb/^{206}Pb$	1σ	$^{206}Pb/^{238}U$(Ma)	1σ
Sample BZ05-1 (potassic trachybasalt)									
1	2004	1727	1.16	169.56	2.32	0.0585	0.0032	37.9	0.5
2	804	667	1.20	169.93	3.04	0.0540	0.0048	37.8	0.7
3	701	500	1.40	169.59	3.92	0.0509	0.0061	37.9	0.9
4	1566	2651	0.59	166.19	2.08	0.0476	0.0024	38.7	0.5
5	1497	1497	1.00	166.40	2.50	0.0505	0.0035	38.6	0.6
6	435	1438	0.30	164.72	2.12	0.0491	0.0034	39.0	0.5
7	1572	1456	1.08	168.21	2.59	0.0457	0.0031	38.2	0.6
8	506	662	0.77	167.19	2.71	0.0471	0.0051	38.4	0.6
9	1124	989	1.14	165.10	2.80	0.0531	0.0042	38.9	0.7
10	548	422	1.30	166.80	3.98	0.0526	0.0073	38.5	0.9
11	747	990	0.75	168.88	2.78	0.0549	0.0040	38.1	0.6
12	617	834	0.74	168.17	2.86	0.0499	0.0057	38.2	0.6
13	395	494	0.80	166.75	3.86	0.0492	0.0062	38.5	0.9
14	677	729	0.93	169.77	3.09	0.0507	0.0050	37.9	0.7
15	503	364	1.38	165.98	3.74	0.0633	0.0083	38.7	0.9
16	966	1140	0.85	172.20	2.64	0.0576	0.0041	37.3	0.6
17	570	470	1.21	159.69	3.06	0.0491	0.0060	40.2	0.8
18	1049	1102	0.95	159.54	3.21	0.0684	0.0050	40.3	0.8
Sample BZ04-2 (shoshonite)									
1	1765	6376	0.28	158.74	1.52	0.0471	0.0017	40.5	0.4
2	968	1014	0.95	165.78	2.75	0.0435	0.0037	38.8	0.6
3	616	972	0.63	161.40	2.87	0.0447	0.0048	39.8	0.7
4	2551	4269	0.60	158.24	1.74	0.0459	0.0020	40.6	0.4
5	2539	5387	0.47	159.43	1.59	0.0471	0.0016	40.3	0.4
6	29,081	2405	12.09	165.16	2.10	0.0488	0.0028	38.9	0.5
7	1310	3670	0.36	159.04	1.42	0.0476	0.0022	40.4	0.4
8	1501	3191	0.47	158.59	1.95	0.0480	0.0021	40.5	0.5
9	1083	4950	0.22	160.16	1.49	0.0493	0.0019	40.1	0.4
10	379	627	0.60	160.31	3.12	0.0566	0.0057	40.1	0.8
11	630	702	0.90	166.60	3.31	0.0451	0.0057	38.6	0.8
Sample BZ03-3 (latite)									
1	1727	3083	0.56	161.59	2.72	0.0524	0.0038	39.8	0.7
2	4037	8834	0.46	163.80	1.81	0.0489	0.0021	39.2	0.4
3	10,196	8504	1.20	162.96	1.83	0.0497	0.0026	39.4	0.4
4	1118	3075	0.36	159.77	2.59	0.0487	0.0040	40.2	0.6
5	969	3116	0.31	162.66	2.42	0.0527	0.0038	39.5	0.6
6	1163	3093	0.38	158.32	2.67	0.0474	0.0045	40.6	0.7
7	1732	5537	0.31	161.24	2.04	0.0452	0.0027	39.9	0.5
8	1674	4438	0.38	162.63	2.20	0.0479	0.0032	39.5	0.5
9	1750	5769	0.30	162.68	1.98	0.0489	0.0031	39.5	0.5
10	713	2294	0.31	159.88	3.25	0.0494	0.0048	40.2	0.8
11	1687	4715	0.36	160.38	2.38	0.0476	0.0030	40.1	0.6
12	2244	6204	0.36	159.22	1.93	0.0514	0.0027	40.4	0.5
13	1089	3527	0.31	163.37	2.73	0.0455	0.0041	39.3	0.7
14	1522	4011	0.38	167.42	2.38	0.0468	0.0034	38.4	0.5

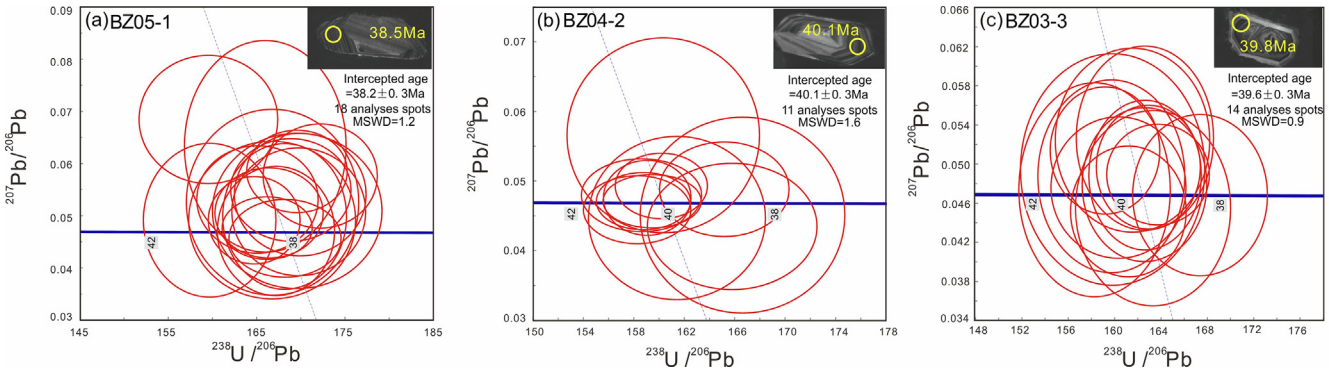

Fig. 4. Zircon U-Pb concordia diagrams for high-Mg potassic volcanic rocks. Potassic trachybasalt (a), shoshonite (b), and latite (c) from Boza area in the Nangqian basin. Illustration shows CL image of representative analyzed zircon grains for in-situ U-Pb isotopes.

Analyses were conducted using a beam diameter of ~55 μm and an 8 Hz repetition rate, resulting in total Hf signals of (1–6) × 10^{-11} A (depending on conditions and Hf contents). Typical ablation times were 60 s, resulting in ablation pits of 40–60 μm with a laser beam energy density of 10 J cm^{-2}. Helium carrier gas transported the ablated aliquot from the laser ablation cell via a mixing chamber to the ICP-MS torch. During laser ablation analyses, the isobaric interference of ^{176}Lu on ^{176}Hf is negligible due to extremely low $^{176}Lu/^{177}Hf$ in zircon

Table 3
Major (wt%) and trace elemental (ppm) concentrations of high-Mg volcanic rocks from Boza area in the Nangqian basin.

Locality	Boza, the Nangqian basin																	
Sample no.	BZ04-5-1	BZ05-1	BZ05-2	BZ05-3	BZ05-4	BZ05-5	BZ05-6	BZ05-7	BZ04-2	BZ04-3	BZ04-5	BZ04-6	BZ04-7	BZ03-3	BZ03-4	BZ03-5	BZ03-6	BZ03-7
Rock type	PTB	PTB	PTB	PTB	PTB	PTB	PTB	PTB	SH	SH	LAT	SH	LAT	LAT	LAT	LAT	LAT	LAT
SiO_2	48.36	48.16	48.04	48.18	48.30	48.38	48.36	48.39	53.88	53.76	53.46	53.94	53.75	56.89	55.93	55.35	55.98	56.18
TiO_2	1.05	1.05	1.05	1.06	1.05	1.05	1.05	1.06	0.93	0.93	0.92	0.93	0.92	0.76	0.78	0.79	0.77	0.79
Al_2O_3	12.85	12.69	12.64	12.59	12.71	12.70	12.73	12.78	13.84	13.76	13.59	13.82	13.7	13.57	13.31	12.99	13.22	13.31
$Fe_2O_3^*$	7.23	7.2	7.14	7.13	7.13	7.18	7.17	7.19	6.09	6.11	6.08	6.09	6.02	5.46	5.72	5.87	5.8	5.49
MnO	0.11	0.11	0.11	0.11	0.11	0.11	0.11	0.11	0.08	0.09	0.08	0.08	0.08	0.07	0.08	0.09	0.08	0.08
MgO	10.17	10.41	10.54	10.34	10.43	10.34	10.37	10.36	6.74	6.81	6.49	6.72	6.79	7.24	7.67	8.4	7.95	7.37
CaO	8.67	8.66	8.59	8.70	8.69	8.74	8.73	8.71	7.29	7.33	7.28	7.24	7.45	6.04	6.4	6.52	6.33	6.15
Na_2O	2.85	2.76	2.75	2.81	2.81	2.83	2.84	2.84	3.58	3.55	3.51	3.53	3.5	3.85	3.75	3.6	3.72	3.78
K_2O	3.36	3.43	3.38	3.40	3.40	3.39	3.36	3.39	4.09	4.07	4.14	4.13	4.11	3.74	3.6	3.4	3.61	3.8
P_2O_5	0.84	0.84	0.84	0.84	0.83	0.85	0.84	0.85	0.77	0.78	0.77	0.78	0.77	0.52	0.53	0.53	0.53	0.55
LOI	3.69	3.72	3.98	3.92	3.93	3.93	3.93	4.03	2.27	2.29	2.26	2.32	2.54	1.32	1.59	1.7	1.45	1.43
Total	99.68	99.5	99.51	99.56	99.87	99.98	100.00	100.20	100.01	99.92	99.02	100.04	100.09	99.87	99.8	99.67	99.86	99.36
Mg#	75	75	76	75	76	75	75	75	70	70	69	70	70	74	74	75	74	74
Cr	329	347	356	395	401	399	388	399	188	197	187	199	200	291	324	367	343	315
Co	42.7	43.3	46	44.3	42.6	42.8	42.6	42.6	44.4	43.4	44.1	47.4	41.5	44.3	48	47.1	47.5	48.4
Ni	237	250	252	276	277	277	271	275	149	154	150	156	152	198	213	239	218	214
Rb	79.0	82.9	85.2	89.1	88.0	91.6	90.4	92.3	104	108	106	111	108	104	99.3	94.3	99.2	109
Sr	1870	1860	1840	1610	1650	1650	1690	1700	1900	1960	1910	2000	1930	1780	1840	1760	1780	1840
Y	18.6	18.5	19.7	19.2	19.1	19.5	19.6	19.7	19.4	19.7	18.9	20.1	19.5	19.2	19.4	19.2	19.1	19.4
Zr	316	321	341	360	359	364	366	364	308	314	307	321	312	288	285	272	284	302
Nb	16.7	16.9	17.8	13.4	13.2	13.3	13.3	13.3	17.2	17.4	17.0	18.1	17.8	17.9	17.0	16.3	16.7	18.1
Ba	1640	1460	1490	1540	1580	1520	1660	1530	1480	1500	1440	1580	1480	1280	1270	1220	1260	1300
Ta	0.723	0.697	0.781	0.793	0.752	0.757	0.778	0.783	0.797	0.834	0.808	0.829	0.845	0.950	0.871	0.861	0.908	0.924
Pb	47.2	20.5	27.0	36.0	38.6	35.2	45.0	28.3	18.4	19.5	17.6	20.5	20.3	20.5	20.1	19.6	21.0	21.7
Th	11.6	11.8	12.6	12.2	12.0	12.1	12.6	12.2	14.7	15.2	14.7	15.8	15.3	14.9	14.4	13.5	14.2	15.1
U	2.94	3.01	3.19	3.22	3.11	3.22	3.17	3.22	3.90	4.09	3.97	4.34	4.24	4.76	4.43	4.09	4.23	4.61
La	85.5	86.8	90.5	88.1	86.9	88.8	89.8	88.6	85.8	88.4	86.0	90.7	88.2	71.9	73.3	70.6	72.7	74.2
Ce	170	171	180	179	177	181	181	181	170	174	171	180	176	142	146	140	143	146
Pr	19.4	19.7	20.6	20.8	20.6	21.1	21.5	21.2	19.6	20.3	19.6	20.8	20.5	16.2	16.6	16.3	16.5	16.6
Nd	74.8	74.6	78.2	75.7	75.6	77.2	78.0	77.4	75.6	76.8	74.9	81.6	77.1	62.2	62.5	61.7	62.6	63.5
Sm	10.9	11.3	11.5	11.5	11.7	11.9	11.8	11.7	11.7	11.9	11.7	12.6	11.7	10	9.95	9.35	9.55	9.73
Eu	2.90	2.94	3.03	2.96	2.95	3.01	3.06	3.03	2.98	3.07	3.06	3.17	3.15	2.53	2.51	2.40	2.45	2.48
Gd	8.39	8.03	8.77	7.99	8.18	8.10	8.12	8.17	8.27	8.45	8.32	8.84	8.38	7.34	6.82	6.93	7.16	7.21
Tb	1.09	1.10	1.15	1.05	1.02	1.05	1.08	1.06	1.10	1.19	1.14	1.18	1.20	1.02	1.07	1.00	0.97	1.00
Dy	3.81	4.01	4.29	4.12	4.03	4.19	4.08	4.08	4.12	4.30	3.91	4.20	4.30	3.97	3.92	3.78	3.86	4.17
Ho	0.68	0.68	0.71	0.75	0.71	0.74	0.75	0.73	0.70	0.74	0.68	0.75	0.70	0.70	0.72	0.68	0.68	0.71
Er	2.13	2.21	2.29	2.04	1.98	2.05	2.05	2.08	2.13	2.23	2.06	2.27	2.17	2.22	2.26	2.23	2.17	2.12
Tm	0.21	0.23	0.24	0.26	0.25	0.25	0.25	0.25	0.22	0.21	0.22	0.24	0.24	0.25	0.26	0.24	0.24	0.26
Yb	1.46	1.50	1.62	1.56	1.57	1.56	1.56	1.55	1.51	1.57	1.45	1.61	1.50	1.69	1.64	1.60	1.72	1.87
Lu	0.230	0.218	0.241	0.225	0.213	0.223	0.218	0.230	0.200	0.248	0.217	0.242	0.222	0.240	0.257	0.246	0.262	0.259
Hf	7.41	7.38	7.90	7.46	7.25	7.74	7.74	7.71	6.92	7.18	7.04	7.49	6.86	6.96	6.82	6.44	7.05	7.60
$[La/Yb]_N$	42.0	41.5	40.1	40.5	39.7	40.8	41.3	41.0	40.8	40.4	42.5	40.4	42.2	30.5	32.1	31.7	30.3	28.5
$[Er/Yb]_N$	1.46	1.47	1.41	1.34	1.30	1.35	1.35	1.38	1.41	1.42	1.42	1.41	1.45	1.31	1.38	1.39	1.26	1.13

Abbreviations: LAT = latite; PTB = potassic trachybasalt; SH = shoshonite. Mg-number = 100 × Mg/(Mg + Fe^{2+}), calculated assuming $Fe_2O_3/(FeO + Fe_2O_3) = 0.15$. * Total Fe is given as Fe_2O_3.

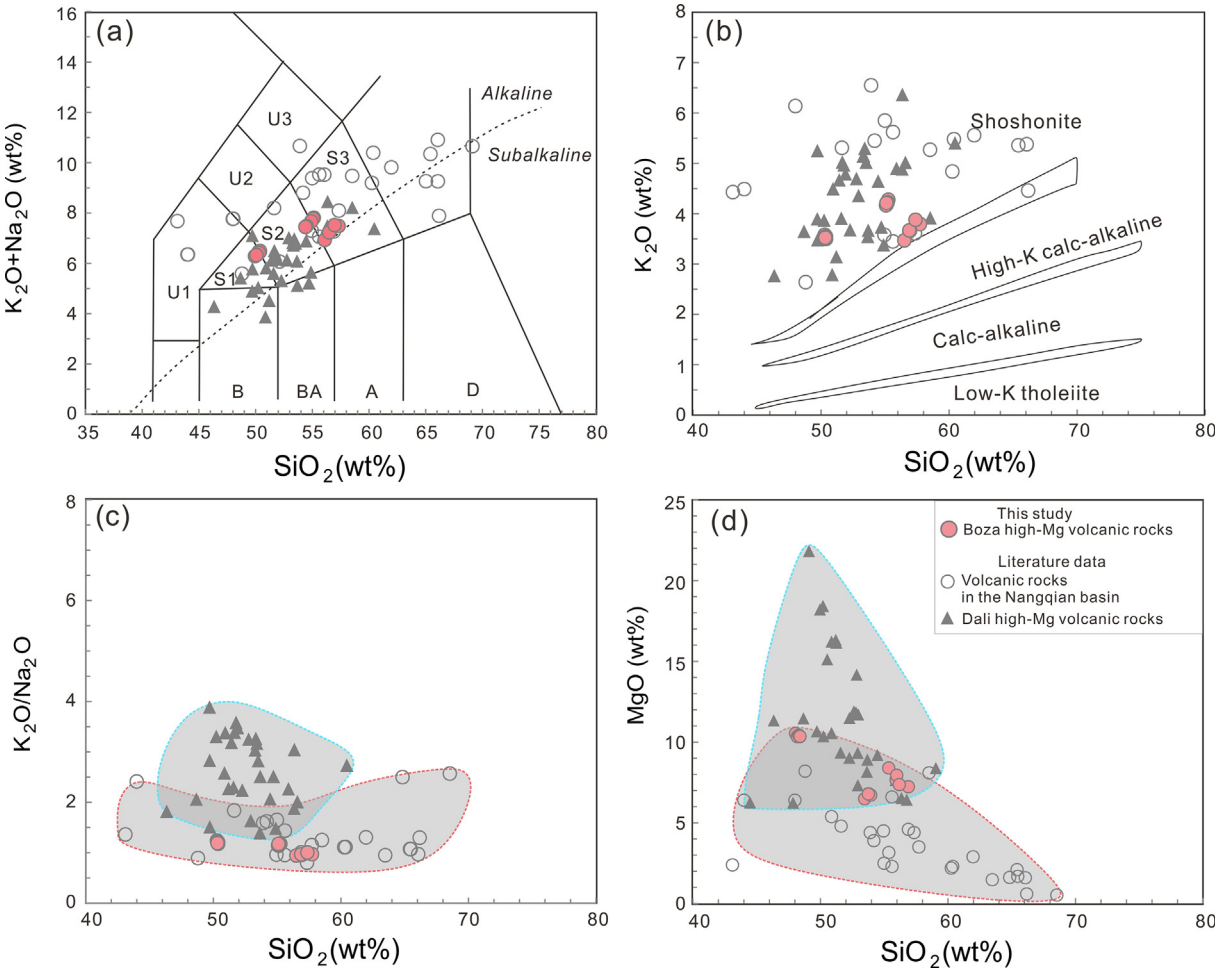

Fig. 5. Geochemical classification of high-Mg potassic volcanic rocks in the Nangqian basin. (a) TAS diagram (Le Maitre et al., 1989); the dashed line separating alkaline series from subalkaline series is from Irvine and Baragar (1971). (b and c) K_2O, K_2O/Na_2O vs. SiO_2, respectively; (d) MgO vs. SiO_2; all the major element values are normalized to 100% on a volatile-free basis. Literature data for the potassic volcanic rocks from the Dali district and the Nangqian basin are shown for comparison. Data source: Dali district: (Huang et al., 2010; Guo et al., 2005; Xu et al., 2001); Nangqian basin: (Spurlin et al., 2005;Sun et al., 2001). U1 = tephrite; U2 = phonotephrite; U3 = tephriphonolite; S1 = potassic trachybasalt; S2 = shoshonite; S3 = latite; T = trachyte; B = basalt; BA = basaltic andesite; A = andesite; D = dacite.

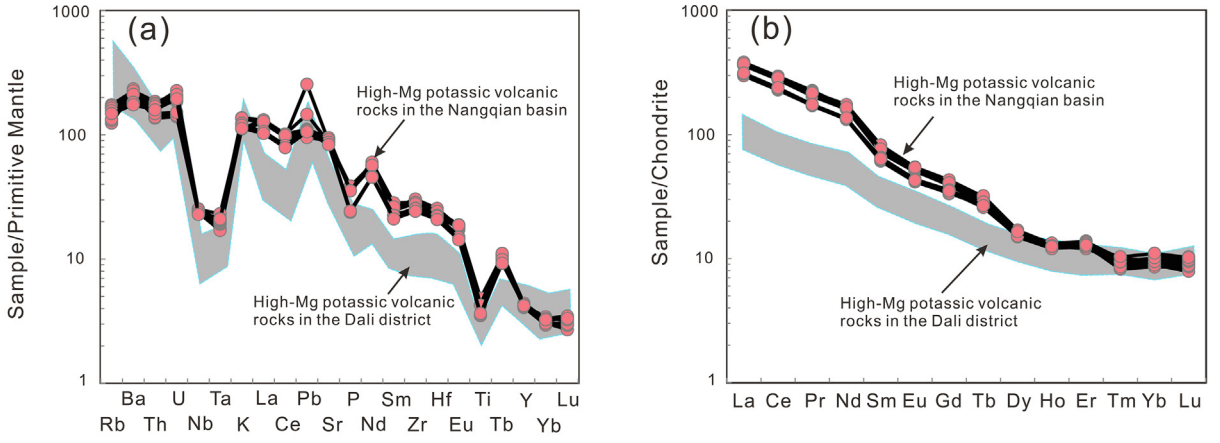

Fig. 6. (a) Primitive mantle normalized multi-element and (b) chondrite-normalized rare earth element patterns diagrams for high-Mg volcanic rocks in the Nangqian basin. The shaded fields represent high-Mg volcanic rocks in the Dali district defined by published data (Huang et al., 2010; Guo et al., 2005; Xu et al., 2001). Chondrite and primitive mantle normalizing values are from Sun and McDonough (1989).

Table 4
Sr-Nd isotopic data of high-Mg volcanic rocks from Boza area in the Nangqian basin.

Sample no.	Rock type	Age (Ma)	$^{87}Rb/^{86}Sr$	$^{87}Sr/^{86}Sr$	± 2σ	$(^{87}Sr/^{86}Sr)i$	$^{147}Sm/^{144}Nd$	$^{143}Nd/^{144}Nd$	± 2σ	$(^{143}Nd/^{144}Nd)_i$	$\varepsilon_{Nd}(t)$	T_{DM} (Ma)
BZ04-5-1	PTB	38.3	0.1223	0.705586	10	0.705521	0.0881	0.512588	3	0.512567	−0.56	682
BZ05-1	PTB	38.3	0.1290	0.705547	12	0.705479	0.0916	0.512593	5	0.512571	−0.49	696
BZ05-2	PTB	38.3	0.1340	0.705559	10	0.705488	0.0889	0.512585	3	0.512563	−0.64	691
BZ03-3	LAT	39.7	0.1691	0.705126	14	0.705034	0.0972	0.512615	1	0.512591	0.04	701
BZ03-4	LAT	39.7	0.1562	0.705114	16	0.705029	0.0963	0.512618	2	0.512594	0.10	691
BZ03-5	LAT	39.7	0.1551	0.705122	10	0.705038	0.0916	0.512615	1	0.512592	0.07	669
BZ03-6	LAT	39.7	0.1613	0.705118	18	0.705030	0.0922	0.512614	1	0.512591	0.04	673
BZ04-2	SH	40.1	0.1584	0.705554	14	0.705472	0.0936	0.512562	1	0.512540	−1.00	747
BZ04-3	SH	40.1	0.1595	0.705523	12	0.705440	0.0937	0.512568	2	0.512546	−0.89	740
BZ04-5	LAT	40.1	0.1606	0.705531	16	0.705448	0.0944	0.512588	1	0.512565	−0.50	719
BZ04-6	SH	40.1	0.1606	0.705537	10	0.705454	0.0934	0.512559	2	0.512537	−1.06	749

$^{87}Rb/^{86}Sr$ and $^{147}Sm/^{144}Nd$ are calculated using whole-rock Rb, Sr, Sm and Nd values in Table 3. Chondritic Uniform Reservoir (CHUR) at the present day [$(^{87}Rb/^{86}Sr)_{CHUR}$ = 0.0847 (McCulloch and Black, 1984); $(^{87}Sr/^{86}Sr)_{CHUR}$ = 0.7045 (DePaolo, 2012); $(^{147}Sm/^{144}Nd)_{CHUR}$ = 0.1967 (Jacobsen and Wasserburg, 1980); $(^{143}Nd/^{144}Nd)_{CHUR}$ = 0.512638 (Goldstein et al., 1984)] was used for the calculations. Nd depleted mantle model ages (T_{DM}) were calculated using $(^{147}Sm/^{144}Nd)_{DM}$ = 0.2137 and $(^{143}Nd/^{144}Nd)_{DM}$ = 0.51315 (Peucat et al., 1989) at the present day. Initial $^{87}Sr/^{86}Sr$ ratios and $\varepsilon_{Nd}(t)$ values are corrected using zircon U-Pb ages. *Abbreviations:* LAT = latite; PTB = potassic trachybasalt; SH = shoshonite.

Table 5
Pb isotopic data of high-Mg volcanic rocks from Boza area in the Nangqian basin.

Sample	Pb	Th	U	$^{206}Pb/^{204}Pb$	2σ	$^{207}Pb/^{204}Pb$	2σ	$^{208}Pb/^{204}Pb$	2σ	$^{238}U/^{204}Pb$	$^{232}Th/^{204}Pb$	t (Ma)	$(^{206}Pb/^{204}Pb)_i$	$(^{207}Pb/^{204}Pb)_i$	$(^{208}Pb/^{204}Pb)_i$
BZ04-5-1	47.2	11.6	2.94	18.697	8	15.522	8	38.504	7	4.60	18.1	38.3	18.670	15.521	38.470
BZ05-1	20.5	11.8	3.01	18.703	6	15.522	4	38.531	8	10.8	42.5	38.3	18.639	15.519	38.450
BZ05-2	27	12.6	3.19	18.742	14	15.535	12	38.561	12	8.70	34.5	38.3	18.690	15.533	38.496
BZ03-3	20.5	14.9	4.76	18.758	12	15.545	8	38.605	12	17.0	53.7	39.7	18.653	15.540	38.499
BZ03-4	20.1	14.4	4.43	18.793	10	15.577	8	38.693	8	16.2	53.1	39.7	18.693	15.572	38.589
BZ03-5	19.6	13.5	4.09	18.775	16	15.559	12	38.623	14	15.3	50.9	39.7	18.680	15.555	38.523
BZ03-6	21	14.2	4.23	18.792	14	15.579	12	38.687	12	14.8	50.1	39.7	18.700	15.575	38.588
BZ04-2	18.4	14.7	3.9	18.744	12	15.527	6	38.609	7	15.5	59.0	40.1	18.647	15.522	38.492
BZ04-3	19.5	15.2	4.09	18.772	12	15.557	6	38.705	11	15.4	57.7	40.1	18.676	15.552	38.590
BZ04-5	17.6	14.7	3.97	18.793	6	15.567	6	38.708	6	16.6	61.9	40.1	18.690	15.562	38.585
BZ04-6	20.5	15.8	4.34	18.788	8	15.555	6	38.667	7	15.6	57.0	40.1	18.691	15.550	38.554

Note: (1) $^{238}U/^{204}Pb$ and $^{232}Th/^{204}Pb$ ratios are calculated by using measured whole-rock Pb, Th and U contents (Table 3) and present-day whole-rock Pb isotopic ratios; (2) Initial Pb isotopic ratios were obtained by using the zircon U-Pb ages of the volcanic rocks (Table 2).

(generally < 0.002), whereas the interference of ^{176}Yb on ^{176}Hf was carefully corrected using independent mass bias factors for Hf and Yb. Detailed instrumental conditions and isobaric interference corrections were described by Wu et al. (2006). In this study, four zircon standards, including Mud Tank, 91500, Temora, and GJ-1, were analyzed to evaluate the accuracy of the laser ablation results. During all analyses, a weighted mean of $^{176}Hf/^{177}Hf$ of 0.282509 ± 20 (2σ, n = 48) and 0.282305 ± 18 (2σ, n = 20) was measured for the Zircon Mud Tank and 91500 standards (the recommended values are 0.282530 ± 30 and 0.282307 ± 31, respectively) (Griffin et al., 2006; Wu et al., 2006), Temora gave a mean $^{176}Hf/^{177}Hf$ of 0.282684 ± 18 (2σ, n = 20) (the recommended value is 0.282307 ± 31) (Wu et al., 2006), and GJ-1 yielded a mean $^{176}Hf/^{177}Hf$ of 0.282006 ± 24 (2σ, n = 20) (the recommended value is 0.282008 ± 18) (Gerdes and Zeh, 2006). Initial Hf isotopic ratios were calculated with reference to the chondritic reservoir at the time of magma crystallization that corresponds to the age of zircon growth from the magma. A decay constant of 1.865×10^{-11} yr^{-1} for ^{176}Lu (Scherer et al., 2001), and the chondritic ratios for $^{176}Hf/^{177}Hf$ (0.282772) and $^{176}Lu/^{177}Hf$ (0.0332) given by Blichert-Toft and Albarède (1997) were adopted in this study. These values were reported relative to the $^{176}Hf/^{177}Hf$ of 0.282163 for the JMC475 standard. Hf depleted model ages (T_{DM}) were calculated using the measured $^{176}Lu/^{177}Hf$ and $^{176}Hf/^{177}Hf$, referring to a model of a depleted mantle with a present-day $^{176}Hf/^{177}Hf$ of 0.28325, similar to that of average MORB (Nowell et al., 1998), and a $^{176}Lu/^{177}Hf$ of 0.0384 (Griffin et al., 2002). This is similar, though not identical, to the depleted mantle curve defined by juvenile rocks through time.

4.6. Electron microprobe analyses

The elemental analyses of pyroxene phenocrysts were acquired from polished thin sections using a JEOL JXA-8230 electron microprobe at Testing Center of Shandong Bureau of China Metallurgy and Geology, China. Element determinations (Si, Mg, Fe, Al, K, Na, Ti, Ca, Ni, Mn, Cr, Ti) of pyroxene were carried out using a beam size of 5 μm, an accelerating potential voltage of 15 kV, and a probe current of 15nA. AS 02753-AB 53 minerals standard from American SPI supplies (www.2spi.com) were used as the standards for Si, Mg, Fe, Al, K, Na, Ca, Ni, Mn, Cr, Ti, such as jadeite for Si, olivine for Mg and Fe and diopside for Ca. Matrix effects were corrected using the ZAF software provided by JEOL. The accuracy of the reported values for the analyses is 1–5% depending on the abundance of the element.

5. Results

5.1. Zircon LA-ICP-MS U-Pb ages

Zircon U-Pb isotopic results for Boza high-Mg volcanic rocks are listed in Table 2. Cathodoluminescence (CL) images show that these zircon grains are dominated by colorless euhedral and prismatic crystals with clear igneous oscillatory zoning (Fig. 4). Sparse zircon xenocrysts have irregular or rounded shapes. Diameters of zircon crystals vary from 50 to 100 μm. The analyzed zircons are mostly idiomorphic crystals with clear magmatic oscillatory zoning. They have a wide range of Th (379–29081 ppm) and U (364–8834 ppm) concentrations. Most analyses have Th/U ratios of 0.22–1.4, except for one analysis (BZ04-2, spot 6) with a higher ratio of 12.09, indicative of a magmatic origin.

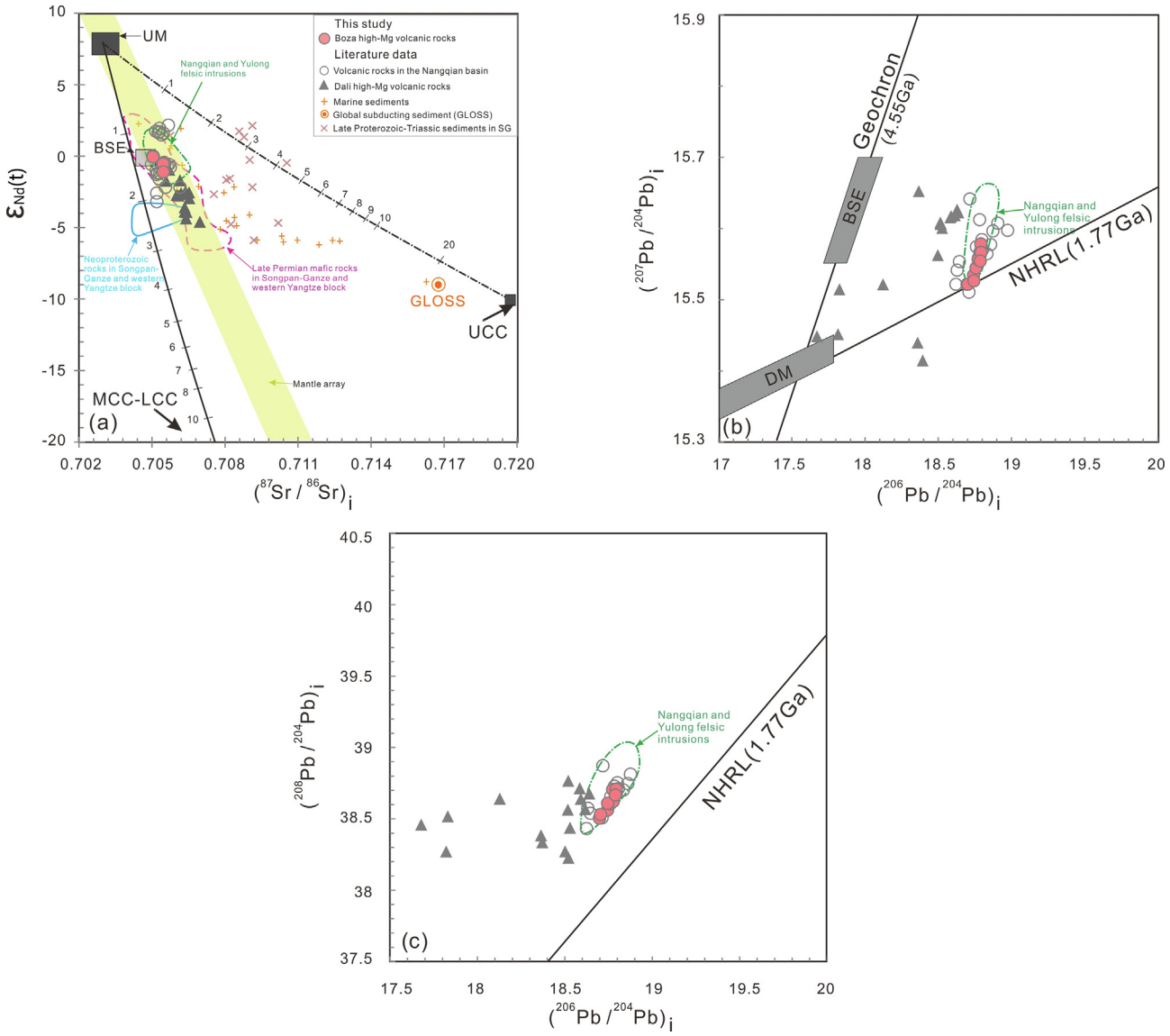

Fig. 7. (a) εNd(t) vs $(^{87}Sr/^{86}Sr)_i$; (b) $(^{207}Pb/^{204}Pb)_i$ vs $(^{206}Pb/^{204}Pb)_i$; (c) $(^{208}Pb/^{204}Pb)_i$ vs $(^{206}Pb/^{204}Pb)_i$. The NHRL (Northern Hemisphere Reference Line; Hart, 1984), mantle array (Hart et al., 1986), and the bulk solid earth (BSE; Zindler and Hart, 1986) are shown for reference. The dot-dash lines is a mixing curve between upper mantle peridotites (UM) (Taylor and McLennan, 1985; $^{87}Sr/^{86}Sr = 0.703$, Sr = 20 ppm, εNd = 8, and Nd = 1.2 ppm) and upper continental crust (UCC) (Taylor and McLennan, 1985; $^{87}Sr/^{86}Sr = 0.720$, Sr = 350 ppm, εNd = −10, and Nd = 26 ppm); the solid line is a mixing curve between UM and middle to low crust (MCC-LCC) (Rudnick and Fountain, 1995; $^{87}Sr/^{86}Sr = 0.710$, Sr = 300 ppm, εNd = −30, and Nd = 24 ppm). Isotope data for the Nangqian and Yulong felsic intrusions (Xu et al., 2016; Jiang et al., 2006), high-Mg potassic volcanic rocks in the Dali district (Huang et al., 2010; Guo et al., 2005; Xu et al., 2001), the Neoproterozoic igneous and metamorphic rocks in the Songpan–Ganze and western Yangtze blocks (Li et al., 2003; Roger and Calassou, 1997), the Proterozoic–-Triassic sediments in the Songpan–Ganze block (Chen et al., 2006; She et al., 2006), Late Permian mafic rocks in the Songpan–Ganze and western Yangtze blocks (Xu et al., 2001; Song et al., 2004), marine sediments and GLOSS (global subducting sediment; Plank and Langmuir, 1998) were plotted for comparison.

The data are plotted on a Tera–Wasserburg diagram (Tera and Wasserburg, 1972), with an anchoring point of $^{207}Pb/^{206}Pb = 0.83 \pm 0.6$ (ratio of average crust composition; Anderson, 2002). Analyzed zircon grains from samples BZ05-1, BZ04-2, and BZ03-3 yielded intercept ages of 38.2 ± 0.3 Ma (2σ, MSWD = 1.2, n = 18), 40.1 ± 0.3 Ma (2σ, MSWD = 1.6, n = 11) and 39.6 ± 0.3 Ma (2σ, MSWD = 0.9, n = 14), which is consistent with the weighted mean $^{206}Pb/^{238}U$ ages of 38.5 ± 0.4 Ma (2σ, MSWD = 1.2, n = 18), 40.1 ± 0.4 Ma (2σ, MSWD = 1.8, n = 11) and 39.6 ± 0.3 Ma (2σ, MSWD = 1.0, n = 14), respectively.

5.2. Major and trace elements

Major and trace elemental results of Boza potassic rocks are presented in Table 3. They vary from potassic trachybasalts to latites (MgO = 6.49–10.54 wt%; SiO_2 = 48.04–56.89 wt%) with high Mg-numbers (Mg#) ranging from 69 to 75 [Mg# = molar Mg × 100/(Mg + Fe^{2+})] (Fig. 5; Table 3). In the total alkalis-silica diagram (Le Maitre et al., 1989; Le Bas et al., 1986), all the samples fall into the fields ranging from potassic trachybasalt to shoshonite and latite (Fig. 5a). The rocks are characterized by high K_2O (3.36–4.14 wt%) and relatively low Na_2O (2.75–3.85 wt%) contents with K_2O/Na_2O ratios of 0.94–1.24 (Fig. 5b and c). In terms of trace elements, they show enrichment of the LREE and LILE relative to HREE and HFSE with steep chondrite-normalized REE patterns [$(La/Yb)_N$ = 28.46–42.54, $(Er/Yb)_N$ = 1.16–1.51], and exhibit negative anomalies of Nb, Ta, Ti, and P (Fig. 6; Table 3). Moreover, the samples, particularly the potassic trachybasalts, have high contents of compatible elements such as Cr (187–367 ppm) and Ni (149–252 ppm, Table 3).

Table 6
Hf isotopic data for the magmatic zircons of high-Mg volcanic rocks, Boza area of the Nangqian basin.

Spots	$^{176}Yb/^{177}Hf$	$^{176}Lu/^{177}Hf$	$^{176}Hf/^{177}Hf$	1 σ	$\varepsilon_{Hf}(t)$	1σ	T_{DM} (Ma)	1σ
BZ05-1 (potassic trachybasalt; 38.31 ± 0.31 Ma)								
1	0.032796	0.001050	0.282917	0.000012	5.96	0.44	475	18
2	0.033564	0.001086	0.282950	0.000011	7.12	0.38	429	15
3	0.032679	0.001100	0.282966	0.000013	7.67	0.47	407	19
4	0.038212	0.001093	0.282956	0.000013	7.33	0.47	421	19
5	0.038887	0.001133	0.282937	0.000011	6.65	0.40	448	16
6	0.042003	0.001512	0.282925	0.000014	6.22	0.48	470	20
7	0.037566	0.001177	0.282900	0.000011	5.32	0.39	502	16
8	0.033910	0.001044	0.282967	0.000012	7.72	0.41	404	17
9	0.027783	0.000852	0.282876	0.000011	4.51	0.39	531	15
10	0.032682	0.000999	0.282939	0.000010	6.71	0.35	444	14
11	0.038026	0.001122	0.282928	0.000011	6.32	0.38	461	15
12	0.037947	0.001155	0.282874	0.000010	4.41	0.35	539	14
13	0.031720	0.000972	0.282947	0.000010	7.00	0.35	433	14
14	0.036114	0.001077	0.282905	0.000011	5.51	0.40	494	16
15	0.037211	0.001122	0.282892	0.000012	5.05	0.43	513	17
16	0.041908	0.001280	0.282890	0.000010	5.00	0.34	517	14
17	0.036897	0.001266	0.282903	0.000014	5.45	0.49	499	20
18	0.035177	0.001085	0.282937	0.000009	6.65	0.33	448	13
BZ04-2 (shoshonite; 40.09 ± 0.43 Ma)								
1	0.051221	0.001894	0.282945	0.000011	6.94	0.39	446	16
2	0.042009	0.001515	0.282975	0.000012	8.03	0.41	398	17
3	0.061984	0.001824	0.282869	0.000015	4.27	0.53	555	22
4	0.038554	0.001223	0.282901	0.000010	5.42	0.34	500	14
5	0.037219	0.001336	0.282902	0.000009	5.44	0.31	501	12
6	0.022169	0.000620	0.282981	0.000007	8.24	0.25	381	10
7	0.093638	0.003178	0.282922	0.000017	6.12	0.61	496	26
8	0.088817	0.002842	0.282864	0.000009	4.07	0.30	578	13
9	0.061899	0.002078	0.282975	0.000010	8.01	0.37	404	15
10	0.068591	0.002253	0.282940	0.000008	6.75	0.27	458	11
11	0.048435	0.001629	0.282941	0.000010	6.80	0.35	449	14
12	0.036830	0.001135	0.282917	0.000010	5.99	0.36	476	14
13	0.028987	0.000896	0.282944	0.000009	6.95	0.32	435	13
14	0.053673	0.001877	0.282912	0.000007	5.77	0.25	494	10
15	0.055325	0.001714	0.282896	0.000008	5.21	0.29	515	12
16	0.051774	0.001812	0.282897	0.000009	5.26	0.33	514	14
17	0.028670	0.000911	0.282930	0.000008	6.46	0.30	455	12
18	0.091320	0.002897	0.282955	0.000008	7.28	0.28	443	12
BZ03-3 (latite; 39.74 ± 0.30 Ma)								
1	0.040324	0.001207	0.282921	0.000009	6.10	0.33	473	13
2	0.040461	0.001215	0.282918	0.000010	6.00	0.35	477	14
3	0.032315	0.000983	0.282978	0.000011	8.14	0.37	388	15
4	0.038498	0.001177	0.282964	0.000010	7.63	0.34	410	14
5	0.054605	0.001567	0.282965	0.000010	7.67	0.36	413	15
6	0.036344	0.001151	0.282944	0.000010	6.94	0.36	438	15
7	0.034985	0.001110	0.282927	0.000011	6.31	0.39	463	16
8	0.032006	0.001030	0.282905	0.000011	5.55	0.38	493	15
9	0.043886	0.001353	0.282883	0.000011	4.75	0.40	529	16
10	0.032878	0.001096	0.282945	0.000010	6.96	0.35	437	14
11	0.042596	0.001390	0.282958	0.000011	7.41	0.37	422	15
12	0.038950	0.001340	0.282955	0.000011	7.31	0.37	425	15
13	0.041365	0.001289	0.282944	0.000011	6.91	0.38	441	15
14	0.037562	0.001258	0.282974	0.000011	7.97	0.41	397	16
15	0.038315	0.001247	0.283014	0.000011	9.40	0.40	339	16
16	0.038007	0.001237	0.282930	0.000012	6.42	0.41	460	17
17	0.037650	0.001228	0.282976	0.000010	8.06	0.34	394	14
18	0.044953	0.001465	0.282950	0.000009	7.11	0.32	434	13
19	0.050420	0.001583	0.282971	0.000010	7.87	0.35	405	14
20	0.041148	0.001319	0.282943	0.000010	6.89	0.37	442	15

$\varepsilon_{Hf}(t) = 10000[(^{176}Hf/^{177}Hf)_S-(^{176}Lu/^{177}Hf)_S(e^{\lambda t}-1)]/[(^{176}Hf/^{177}Hf)_{CHUR,0}-(^{176}Lu/^{177}Hf)_{CHUR}(e^{\lambda t}-1)]-1$. Values for $(^{176}Hf/^{177}Hf)_{CHUR,0}$ (0.282785) and $(^{176}Lu/^{177}Hf)_{CHUR}$ (0.0336) are from Bouvier et al. (2008). $\varepsilon_{Hf}(t)$ calculated using a Lu decay constant of 1.865×10^{-11} a^{-1} (Scherer et al., 2001). Hf depleted model ages (T_{DM}) were calculated using the measured $^{176}Lu/^{177}Hf$ and $^{176}Hf/^{177}Hf$, referring to a model of a depleted mantle with a present-day $^{176}Hf/^{177}Hf$ of 0.28325 (Nowell et al., 1998) and a $^{176}Lu/^{177}Hf$ of 0.0384 (Griffin et al., 2002).

5.3. Sr-Nd-Pb isotopes

Sr, Nd, and Pb isotope results are presented in Tables 4 and 5, and plotted in Fig. 7. Boza high-Mg volcanic rocks have $(^{87}Sr/^{86}Sr)_i$ ratios of 0.7050–0.7055 and εNd(t) of −1.06–0.10 (Fig. 7a). Their depleted mantle Nd model ages (T_{DM}) range from 0.6 to 0.7 Ga. They have narrow ranges of $(^{206}Pb/^{204}Pb)_i$ (18.63–18.71), $(^{207}Pb/^{204}Pb)_i$ (15.52–15.57), and $(^{208}Pb/^{204}Pb)_i$ (38.42–38.59), plotting well above the Northern Hemisphere Reference Line (NHRL; Fig. 7b and c; Hart, 1984).

5.4. Zircon Hf isotope

Zircon Hf isotopic data are listed in Table 6. The εHf(t) values were

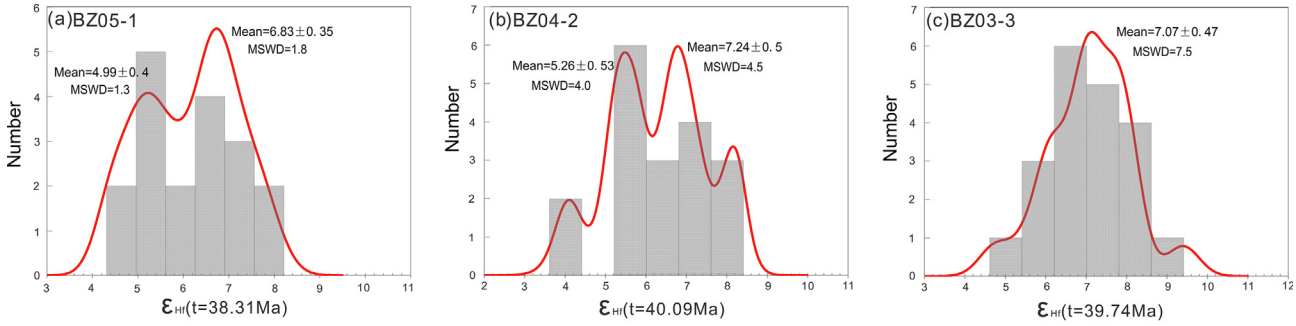

Fig. 8. εHf(t) values of high-Mg potassic volcanic rocks in the Nangqian basin.

Table 7
Summarized zircon U-Pb and Ar-Ar ages of high-Mg volcanic rocks in the Nangqian basin and Dali district.

Locality	Rock type	Analyzed phase	Method	Age (Ma)	Reference
The Nangqian basin					
BZ05-1	PTB	Zrn	LA-ICPMS U-Pb	38.2 ± 0.3	This study
BZ04-2	BTA	Zrn	LA-ICPMS U-Pb	40.1 ± 0.3	This study
BZ03-3	BTA	Zircon	LA-ICPMS U-Pb	39.6 ± 0.3	This study
	SH	Phlogopite	Ar-Ar	~38.7	Pan (1990)
MS99-4-27-(1b)	TA	Biotite	Ar-Ar	37.2 ± 0.1	Spurlin et al., 2005
MS99-4-18-(1)	TD	Biotite	Ar-Ar	37.3 ± 0.2	Spurlin et al., 2005
MS00-5-9-(4)	TD	Biotite	Ar-Ar	37.4 ± 0.1	Spurlin et al., 2005
MS00-5-25-(1)	TD	Biotite	Ar-Ar	37.6 ± 0.1	Spurlin et al., 2005
MS99-4-16-(2)	BTA	Biotite	Ar-Ar	37.7 ± 0.2	Spurlin et al., 2005
MS00-5-9-(3)	TD	Biotite	Ar-Ar	37.7 ± 0.2	Spurlin et al., 2005
MS99-4-15-(3)	TA	Biotite	Ar-Ar	37.8 ± 0.1	Spurlin et al., 2005
MS99-4-28-(1a)	TA	Biotite	Ar-Ar	38.2 ± 0.1	Spurlin et al., 2005
The Dali district					
Wozhong	SH	Whole rock	Ar-Ar	35.5 ± 0.1	Huang et al., 2010
Houshan	PTB	Whole rock	Ar-Ar	36.6 ± 0.2	Huang et al., 2010
Houshan	LAT	Whole rock	Ar-Ar	36.3 ± 0.2	Huang et al., 2010
Wase	SH	Whole rock	Ar-Ar	35.1 ± 0.2	Huang et al., 2010
DP1-1	BTA	Biotite	Ar-Ar	33.3 ± 0.4	Wang et al., 2001
DP19-1	BTA	Biotite	Ar-Ar	34.0 ± 1.2	Wang et al., 2001
G-1(Y86-172)	TA	Whole rock	Ar-Ar	32.9 ± 0.3	Chung et al., 1998
G-1(P9481)	SH	Whole rock	Ar-Ar	30.0 ± 1.1	Chung et al., 1998
G-1(Y86-71)	SH	Whole rock	Ar-Ar	30.5 ± 1.5	Chung et al., 1998
G-1(YN-131)	TA	Biotite	Ar-Ar	32.8 ± 0.2	Chung et al., 1998
G-1(96YN140)	SH	Phlogopite	Ar-Ar	32.9 ± 0.2	Chung et al., 1998
Beiya	MT	Phlogopite	Ar-Ar	34.75 ± 0.05	Guo et al., 2005
Yanyuan	MT	Sanidine	Ar-Ar	32.76 ± 0.06	Guo et al., 2005

Abbreviations: BTA = basaltic trachyandesite; LAT = latite; MT = minette; PTB = potassic trachybasalt; SH = shoshonite; TA = trachy-andesite; TD = trachydacite. In order to overcome the influence of excess argon, all Ar-Ar isochron ages are adopted to represent the time of Cenozoic high-potassic volcanic eruption.

calculated on the basis of the $^{206}Pb/^{238}U$ model ages of individual zircon grain. The three samples from Boza lavas, BZ05-1, BZ04-2, and BZ03-3, have high and consistent zircon εHf(t) values. Their zircon εHf (t) ratios are 4.4–7.7, 4.1–8.2 and 4.8–9.4, corresponding to depleted mantle Hf model ages of 404–539 Ma, 381–578 Ma and 339–529 Ma, respectively (Fig. 8; Table 6).

5.5. Pyroxene compositions

Pyroxene grains occur as euhedral phenocrysts in the Boza high-Mg volcanic rocks (Fig. 3). Their geochemical compositions are presented in Appendix Table A1. Orthopyroxene grains have high MgO (32.25–35.21 wt%) but low FeO (4.33–6.98 wt%) and CaO (0.86–1.82 wt%) contents, consistent with the composition of enstatite ($Wo_{2-3}En_{86-92}Fs_{7-11}$). The clinopyroxene phenocrysts show relatively high CaO (19.15–22.41 wt%) and low MgO (13.35–19.31 wt%) and FeO (3.40–7.76 wt%) contents and are classified as diopside ($Wo_{39-46}En_{40-54}Fs_{6-15}$).

6. Discussion

6.1. Ages of high-Mg volcanic rocks along the JSAS magmatic belt

Three samples BZ05-1, BZ04-2 and BZ03-3, contain zircons with ages of 38.2 ± 0.3 Ma, 40.1 ± 0.3 Ma and 39.6 ± 0.3 Ma, respectively. These new zircon U-Pb age data, together with the published ages of potassic volcanic rocks in the Nangqian basin, have been summarized in Table 7, and described in Fig. 9. Collectively, they define a relatively short duration of potassic volcanism in the Nangqian basin, ranging from 40.1 Ma to 37.2 Ma. In contrast, the volcanic rocks from Dali have ages ranging from 36.6 Ma to 30.0 Ma, slightly younger than their counterparts in the Nangqian basin. Such a younging trend from north to south in the JSAS magmatic belt has already been revealed by felsic intrusions and associated porphyry Cu-Mo mineralization (Lu et al., 2012; Xu et al., 2012). The ages of magmatic emplacement and Cu-Mo mineralization in the Yulong copper belt vary from 43.8 Ma to 35.8 Ma, whereas felsic intrusions and associated porphyry deposits to the south in the western Yunnan region were generated from 36.3 Ma to 33.9 Ma (Lu et al., 2013a; Xu et al., 2012).

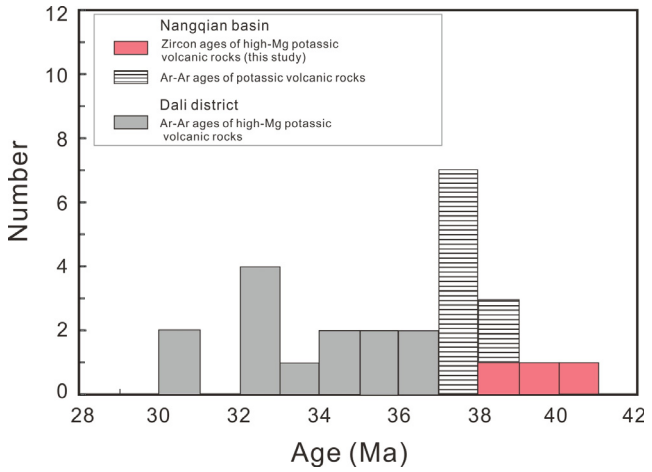

Fig. 9. Age histograms of Eocene–Oligocene high-Mg volcanic rocks along the Jinshajiang–Ailaoshan magmatic belt. Data source: the Ar-Ar ages of volcanic rocks in the Nangqian basin (Spurlin et al., 2005); the Ar-Ar ages of volcanic rocks in the Dali district (Huang et al., 2010; Guo et al., 2005; Wang et al., 2001; Chung et al., 1998).

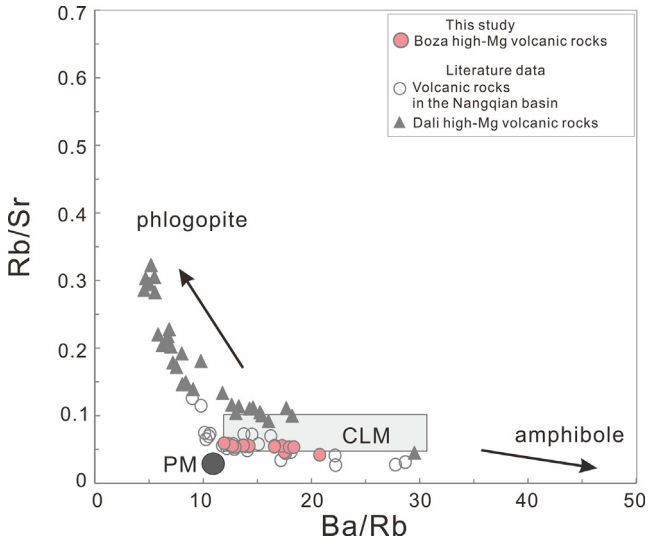

Fig. 10. Diagram of Rb/Sr vs. Ba/Rb. The fields of primitive mantle (PM; Sun and McDonough, 1989) and sub-continental lithospheric mantle (SCLM; Furman and Graham, 1999) were shown for comparison. Qualitative arrows denote the expected compositional variation due to amphibole vs. phlogopite mantle metasomatism, respectively.

6.2. Petrogenesis and magma source of high-Mg potassic volcanic rocks in the Nangqian basin

Volcanic rocks in the Nangqian basin have high contents of MgO (6.5–10.5 wt%; Mg# = 69–75), Cr (188–401 ppm), and Ni (149–277 ppm; Table 3), suggesting that they might be derived from partial melting of sub-continental lithospheric mantle (SCLM; Frey et al., 1978). This is further supported by their positive zircon εHf (t) of 4.1 to 9.4 (Figs. 8 and 11), and relatively high Nd and low Sr isotopic ratios [$(^{87}Sr/^{86}Sr)_i$ = 0.7050–0.7055, εNd(t) of −1.06–0.10; Fig. 7], roughly consistent with the geochemical compositions of SCLM-derived gabbros in the Eastern Qiangtang block (Zi et al., 2012). In a diagram of Ba/Rb vs. Rb/Sr, all samples plot close to the field of SCLM (Fig. 10).

In view of high loss on ignition (LOI) of several samples (Table 3), post-magmatic alteration has to be considered. Mg, Ca and LILEs (e.g. K, Sr, Ba, and Rb) are generally mobile and tend to display a decreasing trend with increasing LOI contents (Q. Wang et al., 2006; Bedard, 1999;

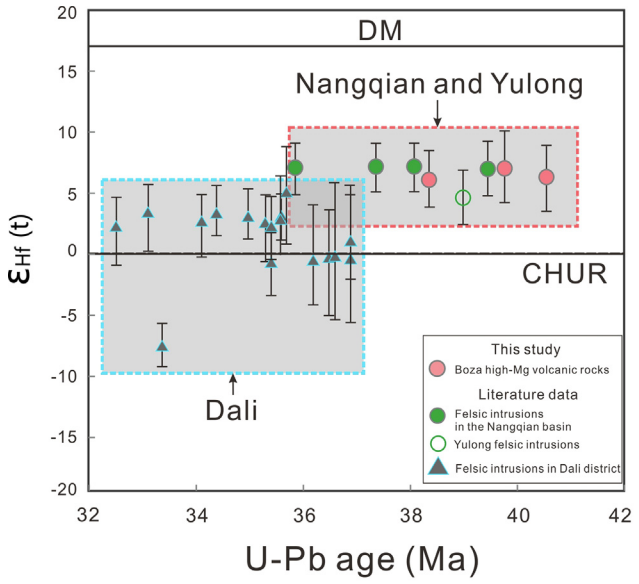

Fig. 11. Variation of initial εHf isotope values vs. U-Pb ages of the zircons. Zircon εHf isotopic values and ages for felsic intrusions in the Nangqian basin were shown for comparison (Xu et al., 2016), the ore-bearing intrusions in the Yulong copper belt (Jiang et al., 2006) and porphyry intrusions in the Dali district (Lu et al., 2013a, b). DM = Depleted Mantle; CHUR = Chondritic Uniform Reservoir.

Smith and Smith, 1976). However, none of these trends have been observed for the studied rocks (Appendix Fig. 1). Thus, the effect of post-magmatic alteration appears to be negligible in the petrogenesis of the high-Mg potassic volcanic rocks in the Nangqian basin.

In the following, we try to assess the effect of crustal contamination during the generation of high-Mg potassic volcanic rocks and their transport to the Earth's surface. As a general rule, high MgO contents probably reflect only limited degrees of crustal contamination (Xu et al., 2017; Guo et al., 2015; Liu et al., 2015; Huang et al., 2010). Appreciable crustal contamination can also be ruled out based on the following observations: (1) all high MgO volcanics have high and uniform Ni and Cr contents (Table 3); (2) the range of $^{206}Pb/^{204}Pb$ ratios is very restricted (Fig. 7b and c); and (3) inherited zircons are absent (Table 2). We will therefore use the geochemical compositions of the high MgO volcanics to reflect on the nature of their mantle source region. In addition, positive correlation between La and La/Yb suggests that partial melting process may have controlled the formation of high-Mg volcanic rock in the Nangqian basin (Fig. 12a).

High-Mg potassic volcanic rocks in the Nangqian basin show negative Nb-Ta-Ti anomalies and elevated LILE and LREE concentrations, probably suggesting the addition of subduction-derived components to the mantle source. This addition can also explain the decoupled Hf-Nd isotopic compositions of these rocks. The global "mantle array" of the Hf-Nd isotopes defined by oceanic basalts is εHf = 1.33εNd + 3.19 (Nowell et al., 2004; Vervoort et al., 1999). Therefore, it is expected that the samples from this study with zircon εHf(t) values of + 4.1–+9.4 have an estimated range of εNd(t) ratios from + 0.7 to + 3.7. This is inconsistent with their measured Nd isotopic composition (εNd(t) = -1.06 to + 0.10; Table 4). An explanation may lie in the fact that LREE (La, Ce, Sm, and Nd) are more soluble than HFSE (e.g., Zr, Hf, Nb, and Ta) in the dehydrating fluids during the slab subduction (Polat and Münker, 2004). This enrichment of Nd relative to Hf during an ancient subduction-related metasomatic process and the time-integrated ingrowth of radiogenic ^{143}Nd and ^{176}Hf should result in a deviation of the Hf-Nd isotopes from the global "mantle array".

Very low HREE contents, steep chondrite-normalized REE patterns

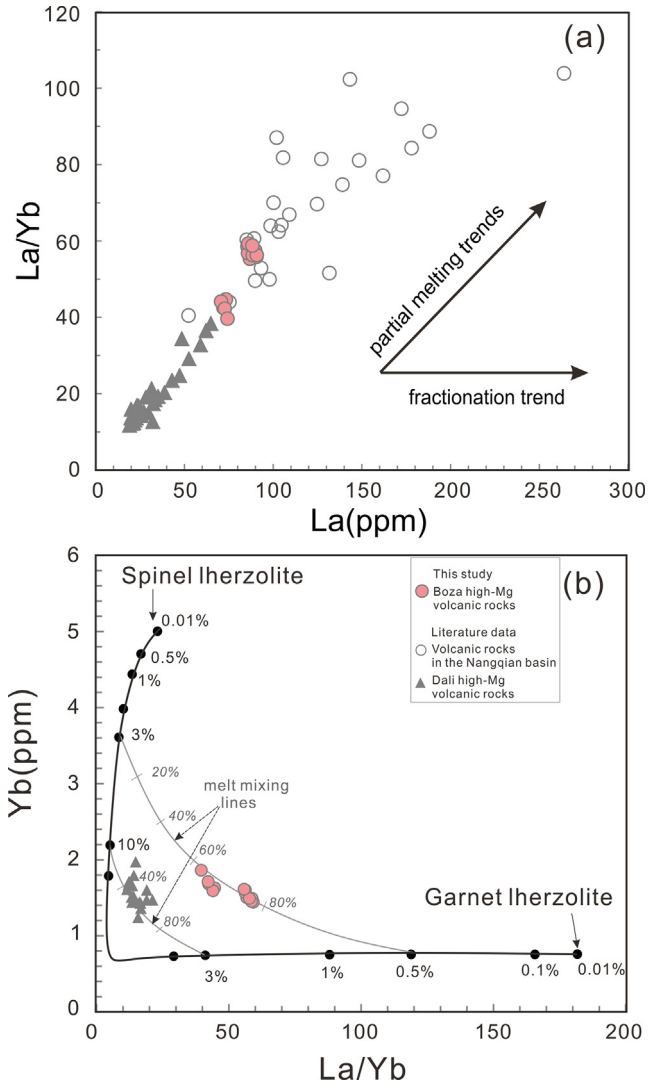

Fig. 12. (a) Plot of La/Yb vs. La for high-Mg potassic volcanic rocks in the Nangqian basin. Fields for volcanic rocks from Dali district are based on the data sources listed in the caption of Fig. 4. (b) Diagram Yb vs. La/Yb. Partial melting trends are indicated for spinel lherzolite and garnet lherzolite mantle sources, calculated using partition coefficients from Irving and Frey (1984) and McKenzie and O'nions (1991). The source modles are from Hellebrand et al. (2002). For spinel lherzolite, the assumed modal source mineralogy is Ol 53 Opx 27 Cpx 17 Sp 3, and weight fractions of liquid contributed by each phase during melting are Ol −6 Opx 28 Cpx 67 Sp 11; for garnet lherzolite, the assumed modal source mineralogy is Ol 57 Opx 21 Cpx 13 Gt 9, and weight fractions of liquid contributed by each phase during melting are Ol 4 Opx −19 Cpx 105 Gt 11. The assumed source composition is La 1.19 ppm and Yb 0.31 ppm, which is the composition of spinel lherzolite inclusions in high-pressure metamorphic rocks from the Eastern Himalayan syntaxis (Namche Barwa; Ding, 1999). High-Mg (Mg# > 70) volcanic rocks from the western Yangtze block are shown for comparison. Numbers beside the mixing curve indicate the weight fraction of the garnet lherzolite end member in the mixture.

($[La/Yb]_N$ = 28.46–42.54), and high Er/Yb ratios (> 1; Fig. 6b; Table 3) suggest that partial melting occurred mainly in the garnet stability field of a peridotitic mantle. A melting trend has relatively high contents of garnet-facies mantle (Fig. 12b).

Therefore, the geochemical characteristics for the high-Mg volcanic rocks in the Nangqian basin can be explained to have derived from a juvenile sub-arc mantle at depths of the garnet stability field. This differs from the interpretation for the Dali occurrences where an older SCLM is the source for the high MgO volcanics and partial melting occurred in the depths of the spinel stability field (Huang et al., 2010; Figs. 11 and 12).

6.3. Heterogeneous SCLM

High-Mg potassic volcanic rocks in the Nangqian basin have juvenile Hf-isotope signatures (εHf(t) = +4.1–+9.4), but most potassic volcanic rocks from the Dali district show ancient Hf-isotope composition (εHf(t) = −9.1–+5.6; Fig. 11). Similarly, Nangqian rocks have more "depleted" Sr-Nd isotopic ratios than their counterparts from Dali (Fig. 7a). The Sr-Nd isotopic compositions of high-Mg potassic volcanic rocks in the Nangqian basin are consistent with their mantle sources that incorporated 1–2% of a continental crustal component. In contrast, the mixing line shows a relatively high crustal contribution (2–3%) for Dali high-Mg volcanic rocks (Fig. 7a). Of particular interest are the higher incompatible trace element ratios (e.g. LILE/HFSE and LILE/LREE) of the Dali high-Mg volcanic rocks compared to those of the Nangqian rocks (Fig. 13). The different geochemical features suggest the different SCLM portions are underlying the two regions along the JSAS magmatic belt.

Heterogeneous SCLM mantle portions may originate by different metasomatic processes at different times. Previous studies have shown that the western margin of the Yangtze block has probably undergone the Neoproterozoic and later Paleozoic subduction events (Sun et al., 2009; Guo et al., 2005; P. Wang et al., 2000). Oceanic subduction for ~100 million years was continuous from 850 to 740 Ma along the western margin of the Yangtze block (Fig. 14a; Zhou et al., 2014). This is also witnessed by potassic-ultrapotassic felsic intrusive rocks in the western Yangtze block that have abundant xenocrystic zircons with U-Pb ages clustering ~840 Ma (Deng et al., 2014b). The Paleozoic subduction formed to the west of the Yangtze block (Fan et al., 2010; Jiang et al., 2006; Guo et al., 2005). There is a debate about the polarity of the Paleo-Tethys Ocean subduction. In light of the Baimaxueshan calc-alkaline pluton (255–248 Ma), the Yaxianqiao arc volcanism (ca. 268–264 Ma), and the Banpo mafic–ultramafic complex (ca. 288–284 Ma) within the Simao block, the westward Paleo-Tethys Ocean subduction is preferred (Zi et al., 2013; Jian et al., 2009). In this model, Paleozoic subduction may not have occurred in the western Yangtze block. Dali high-Mg volcanic rocks have Sr-Nd compositions similar to Neoproterozoic mantle-derived rocks in the western Yangtze block (Fig. 7a) and have Nd model ages of 1.2–1.0 Ga (Huang et al., 2010). Therefore, we propose that the Neoproterozoic subduction rather than Paleozoic subduction caused the dominant Sr-Nd-Pb-Hf isotope enrichment of the SCLM beneath the western Yangtze block. Besides, the long duration of Neoproterozoic subduction (> 100 Ma) may be reflected by the relatively high incompatible trace elements ratios of the high-Mg volcanic rocks (Fig. 13). During the Cenozoic, remelting of the Neoproterozoic metasomatized domains within the SCLM generated the high-Mg potassic volcanic rocks in the Dali district. The melting process may have been triggered by delamination of a thickened crust and upwelling of the asthenosphere beneath the western Yangtze block (Fig. 14b; Deng et al., 2014b; Lu et al., 2013a, 2013b).

The Eastern Qiangtang block might have experienced different metasomatic processes. Evidence from detrital zircon records suggested that the Eastern Qiangtang block was derived from the Indian Gondwana (Tao et al., 2014; Wang et al., 2013; Usuki et al., 2013; Zhu et al., 2013; He et al., 2011; Pullen et al., 2008) rather than the Yangtze block (Metcalfe, 2013, 2002; Zhang et al., 2013). Accordingly, the Neoproterozoic subduction was restricted in the western margin of the Yangtze block, not in the Eastern Qiangtang block. Subduction-related metasomatic enrichment of the SCLM underneath the Eastern Qiangtang block may stem from an Early Permian westwards subduction of the JSAS Paleo-Tethys (Fig. 14c; Deng et al., 2014b; Zi et al., 2013; Fan et al., 2010; Zhao et al., 2009; Jiang et al., 2006). During the Cenozoic time, partial melting of the Permian–Triassic metasomatized domains within SCLM generated high-Mg rocks in the Nangqian basin, induced by continental subduction and subsequent large-scale strike-slip

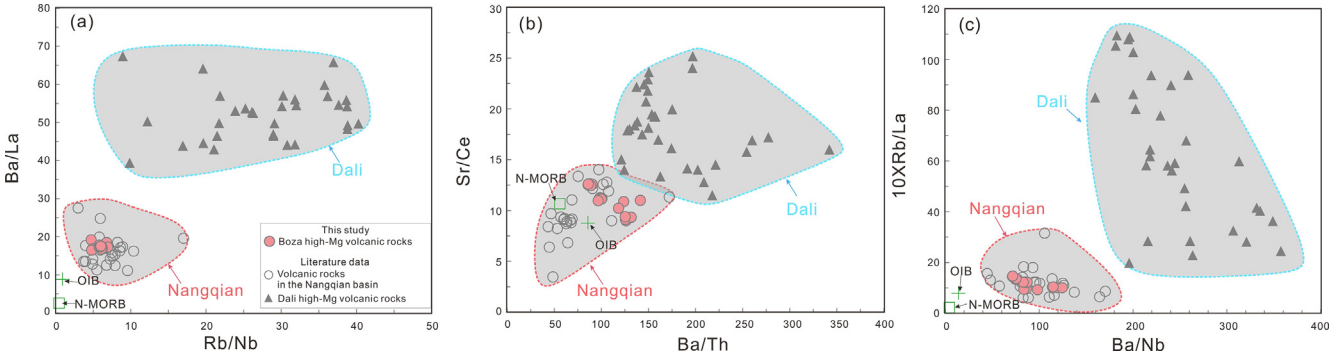

Fig. 13. Diagrams of (a) Ba/La vs. Rb/Nb; (b) Sr/Ce vs. Ba/Th; (c) 10 × Rb/La vs. Ba/Nb. The average composition of N-MORB and ocean island basalts (OIB) is from Sun and McDonough (1989).

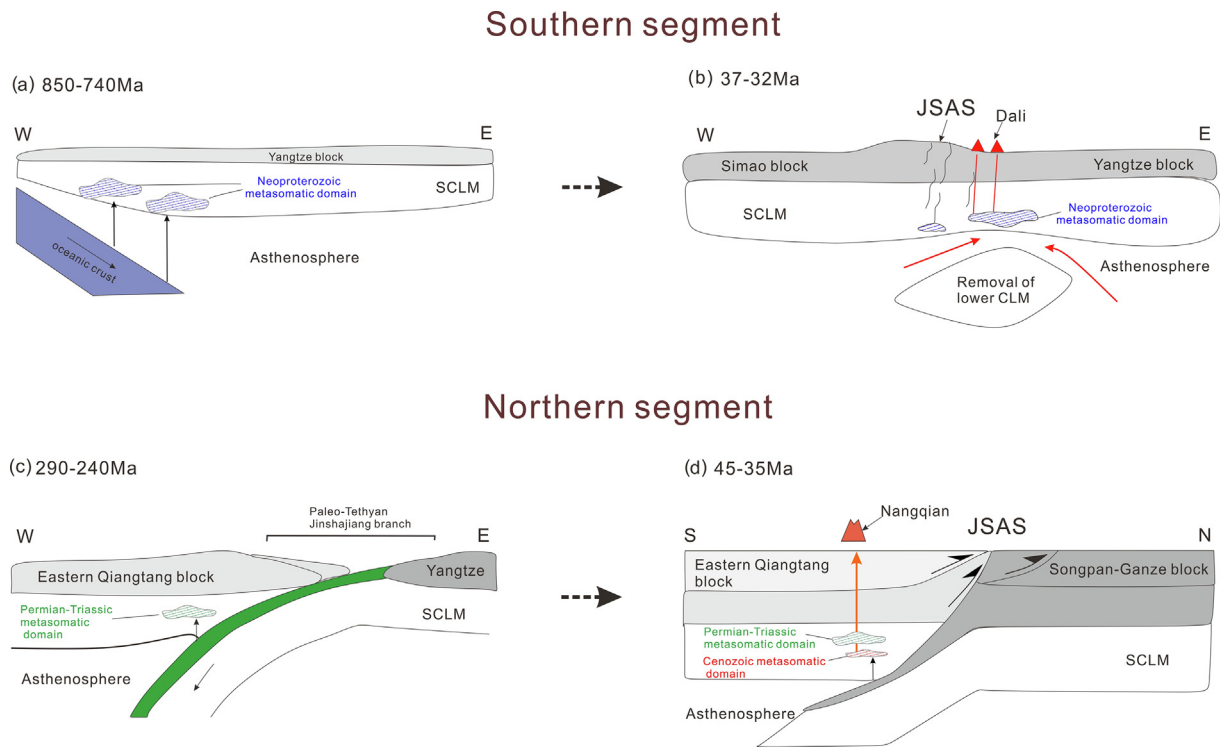

Fig. 14. Schematic illustration of tectonic evolution of the western Yangtze block to the south (a–b) and the Eastern Qiangtang block to the north (c–d) along the JSAS magmatic belt. (a) Oceanic subduction from the western margins of the Yangtze block before 740 Ma produced metasomatic domains within SCLM; (b) the lower overthickened SCLM was removed along the Ailaoshan strike-slip fault at ca. 37–32 Ma (modified from Lu et al., 2013b); (c) Oceanic subduction from the eastern margins of the Eastern Qiangtang block during the latest Permian to earliest Triassic produced metasomatic domains within SCLM (modified from Deng et al., 2014b; Zi et al., 2013); (d) Southward subduction of the Songpan-Ganze block along the Jinshajiang suture created Cenozoic metasomatic domains, and induced remelting of Paleozoic and Cenozoic metasomatic domains within SCLM during the Cenozoic time (modified from Xu et al., 2016).

faulting (Fig. 14d; Xu et al., 2016; Spurlin et al., 2005; Hou et al., 2003; Horton et al., 2002; Tapponnier et al., 2001; Roger et al., 2000).

Another possible enrichment process for the Eastern Qiangtang SCLM may originate from Cenozoic intra-continental subduction. The petrogenesis of the Cenozoic high-K magmas in the Eastern Qiangtang block has been ascribed to the partial melting of enriched lithospheric mantle. Melting was initiated by the southward subducted Songpan–Ganze block (Xu et al., 2016; Wang et al., 2010, 2008; Spurlin et al., 2005; Ding et al., 2003). The SCLM underneath the Eastern Qiangtang block may have been modified by the continental slab subduction of the Songpan–Ganze block as well. Thus, the geochemical characteristic of high-Mg potassic volcanic rocks appear to be a consequence of at least two fluid enrichment events that occurred in the SCLM beneath the Eastern Qiangtang block, i.e. a Paleozoic oceanic slab subduction and a Cenozoic continental subduction (Fig. 14d).

Collectively, high-Mg potassic and ultrapotassic volcanic rocks in the Dali district reveal an ancient, SCLM that was metasomatized by Neoproterozoic oceanic subduction, whereas the high-Mg volcanic rocks in the Nangqian basin were derived directly by partial melting of a juvenile, isotopically “depleted” SCLM metasomatized by Palaeozoic oceanic and Cenozoic continental subduction. Different metasomatic processes resulted in systematic changes of incompatible trace element ratios between these high-Mg lavas from Nangqian and Dali along the JSAS magmatic belt.

7. Conclusions

High-Mg volcanic rocks from the Nangqian basin and Dali district along the JSAS magmatic belt show different geochemical compositions, probably reflecting mantle heterogeneity in a continental post-collision setting from the middle Eocene to the Early Oligocene. High-Mg potassic volcanic rocks in the Nangqian basin were derived directly

by partial melting of a juvenile, isotopically “depleted”, and garnet facies-dominated peridotitic mantle caused by continental subduction and subsequent large-scale strike-slip faulting. In contrast, high-Mg potassic and ultrapotassic volcanic rocks in the Dali district are considered to be derived from melting of an ancient, isotopically “enriched”, and spinel facies-dominated mantle region trigged by lithosphere thinning. SCLM underneath the Eastern Qiangtang block was predominantly metasomatized by Palaeozoic oceanic subduction and Cenozoic continental subduction. However, enrichments of isotopic composition and incompatible trace elements of high-Mg rocks from the western Yangtze block were originated from the long duration of Neoproterozoic oceanic subduction.

Declaration of Competing Interest

We declare that we have no financial and personal relationships with other people or organizations that can inappropriately influence our work. There is no professional or other personal interest of any nature or kind in any product, service and/or company that could be construed as influencing the position presented in or the review of the manuscript entitled.

Acknowledgments

This study was jointly supported by the Strategic Priority Research Program (B) of Chinese Academy of Sciences, China (Grant No. XDB18000000), 13th Five-Year Plan Program of the China Ocean Mineral Resources Research and Development Association Research, China (DY135-S2-2-08), the National Natural Science Foundation Project of China, China (41673049 and 41303040), the China Postdoctoral Science Foundation, China (2017M610403), and the Taishan Scholar Project Funding, China (No. tspd20161007). We thank the staff from the Yunnan Copper Industry Co. Ltd. and the Tibet Yulong Copper Industry Co. Ltd for assistance in the field, and Professor Zhaochu Hu (China University of Geosciences, Wuhan) for LA-ICP-MS zircon analyses. We appreciate the editorial suggestions and English polishing from Prof. Mei-Fu Zhou, and constructive reviews from Prof. Gerhard Brey (Goethe University, Frankfurt, Germany) and two anonymous referees, which were very helpful to improve the manuscript.

Appendix A. Supplementary material

Supplementary data to this article can be found online at https://doi.org/10.1016/j.jseaes.2019.04.018.

References

Anderson, T., 2002. Correction of common lead in U-Pb analyses that do not report ^{204}Pb. Chem. Geol. 192, 59–79.
Bédard, J., 1999. Petrogenesis of boninites from the Betts Cove ophiolite, Newfoundland, Canada: identification of subducted source components. J. Petrol. 40, 1853–1889.
Bi, X., Hu, R., Cornell, D.H., 2004. The alkaline porphyry associated Yao’an gold deposit, Yunnan, China: rare earth element and stable isotope evidence for magmatic-hydrothermal ore formation. Miner. Deposita 39, 21–30.
Blichert-Toft, J., Albarède, F., 1997. The Lu-Hf isotope geochemistry of chondrites and the evolution of the mantle-crust system. Earth Planet. Sci. Lett. 148, 243–258.
Bouvier, A., Vervoort, J.D., Patchett, P.J., 2008. The Lu-Hf and Sm-Nd isotopic composition of CHUR: constraints from unequilibrated chondrites and implications for the bulk composition of terrestrial planets. Earth Planet. Sci. Lett. 273, 48–57.
Chen, Y.-L., Tang, J.-R., Liu, F., Zhang, H.-F., Nie, L.-S., Jiang, L.-T., 2006. Elemental and Sm-Nd isotopic geochemistry of clastic sedimentary rocks in the Garzê-Songpan block and Longmen Mountains. Geol. China 33, 109–118 (in Chinese with English abstract).
Chung, S.-L., Chu, M.-F., Zhang, Y., Xie, Y., Lo, C.-H., Lee, T.-Y., Lan, C.-Y., Li, X., Zhang, Q., Wang, Y., 2005. Tibetan tectonic evolution inferred from spatial and temporal variations in post-collisional magmatism. Earth Sci. Rev. 68, 173–196.
Chung, S.-L., Lo, C.-H., Lee, T.-Y., Zhang, Y., Xie, Y., Li, X., Wang, K.-L., Wang, P.-L., 1998. Diachronous uplift of the Tibetan plateau starting 40 Myr ago. Nature 394, 769–773.
Conticelli, S., Guarnieri, L., Farinelli, A., Mattei, M., Avanzinelli, R., Bianchini, G., Boari, E., Tommasini, S., Tiepolo, M., Prelević, D., 2009. Trace elements and Sr-Nd-Pb isotopes of K-rich, shoshonitic, and calc-alkaline magmatism of the Western Mediterranean Region: genesis of ultrapotassic to calc-alkaline magmatic associations in a post-collisional geodynamic setting. Lithos 107, 68–92.
Deng, W., Huang, X., Zhong, D., 1998. Alkali-rich porphyry and its relation with intraplate deformation of north part of Jinsha River belt in western Yunnan, China. Sci. China, Ser. D Earth Sci. 41, 297–305.
Deng, W., Sun, H., Zhang, Y., 2000. Cenozoic K-Ar ages of volcanic rocks in the Nangqian Basin, Qinghai. Chin. Sci. Bull. 44, 2554–2558 (in Chinese with English abstract).
Deng, J., Wang, Q., Li, G., Li, C., Wang, C., 2014a. Tethys tectonic evolution and its bearing on the distribution of important mineral deposits in the Sanjiang region, SW China. Gondwana Res. 26, 419–437.
Deng, J., Wang, Q., Li, G., Santosh, M., 2014b. Cenozoic tectono-magmatic and metallogenic processes in the Sanjiang region, southwestern China. Earth Sci. Rev. 138, 268–299.
Ding, L., 1999. Cenozoic collisional deformation and lithosphere tectonic evolution of the Eastern Himalayan syntaxis. Ph.D. dissertation, Institute of Geology and Geophysics, Chinese Academy of Sciences, Beijing, pp. 47–59.
DePaolo, D.J., 2012. Neodymium Isotope Geochemistry: An Introduction. Springer Science & Business Media.
Ding, L., Kapp, P., Zhong, D., Deng, W., 2003. Cenozoic volcanism in Tibet: evidence for a transition from oceanic to continental subduction. J. Petrol. 44, 1833–1865.
Ding, L., Maksatbek, S., Cai, F., Wang, H., Song, P., Ji, W., Xu, Q., Zhang, L., Muhammad, Q., Upendra, B., 2017. Processes of initial collision and suturing between India and Asia. Sci. China Earth Sci. 60, 635–651.
Ding, L., Qasim, M., Jadoon, I.A., Khan, M.A., Xu, Q., Cai, F., Wang, H., Baral, U., Yue, Y., 2016. The India-Asia collision in north Pakistan: insight from the U-Pb detrital zircon provenance of Cenozoic foreland basin. Earth Planet. Sci. Lett. 455, 49–61.
Fan, W., Wang, Y., Zhang, A., Zhang, F., Zhang, Y., 2010. Permian arc-back-arc basin development along the Ailaoshan tectonic zone: geochemical, isotopic and geochronological evidence from the Mojiang volcanic rocks, Southwest China. Lithos 119, 553–568.
Foley, S.F., Venturelli, G., Green, D., Toscani, L., 1987. The ultrapotassic rocks: characteristics, classification, and constraints for petrogenetic models. Earth Sci. Rev. 24, 81–134.
Frey, F., Green, D., Roy, S., 1978. Integrated models of basalt petrogenesis: a study of quartz tholeiites to olivine melilitites from south eastern Australia utilizing geochemical and experimental petrological data. J. Petrol. 19, 463–513.
Fu, Y., Sun, X.M., Hollings, P., Li, D.F., Yang, T.J., 2018. Geochronology and trace element geochemistry of titanite in the Machangqing Cu-Mo-dominated polymetallic deposit, Yunnan Province, southwest China. J. Asian Earth Sci. 158, 398–414.
Furman, T., Graham, D., 1999. Erosion of lithospheric mantle beneath the East African Rift system: geochemical evidence from the Kivu volcanic province. Develop. Geotect. 24, 237–262.
Gerdes, A., Zeh, A., 2006. Combined U-Pb and Hf isotope LA-(MC-) ICP-MS analyses of detrital zircons: comparison with SHRIMP and new constraints for the provenance and age of an Armorican metasediment in Central Germany. Earth Planet. Sci. Lett. 249, 47–61.
Goldstein, S., O'nions, R., Hamilton, P., 1984. A Sm-Nd isotopic study of atmospheric dusts and particulates from major river systems. Earth Planet. Sci. Lett. 70, 221–236.
Griffin, W., Pearson, N., Belousova, E., Saeed, A., 2006. Comment: Hf-isotope heterogeneity in zircon 91500. Chem. Geol. 233, 358–363.
Griffin, W., Wang, X., Jackson, S., Pearson, N., O'Reilly, S.Y., Xu, X., Zhou, X., 2002. Zircon chemistry and magma mixing, SE China: in-situ analysis of Hf isotopes, Tonglu and Pingtan igneous complexes. Lithos 61, 237–269.
Guo, Z., Wilson, M., Zhang, M., Cheng, Z., Zhang, L., 2015. Post-collisional ultrapotassic mafic magmatism in South Tibet: products of partial melting of pyroxenite in the mantle wedge induced by roll-back and delamination of the subducted Indian continental lithosphere slab. J. Petrol. 56, 1365–1406.
Guo, Z., Wilson, M., Liu, J., Mao, Q., 2006. Post-collisional, potassic and ultrapotassic magmatism of the northern Tibetan Plateau: Constraints on characteristics of the mantle source, geodynamic setting and uplift mechanisms. J. Petrol. 47, 1177–1220.
Guo, Z., Hertogen, J., Liu, J., Pasteels, P., Boven, A., Punzalan, L., He, H., Luo, X., Zhang, W., 2005. Potassic magmatism in western Sichuan and Yunnan provinces, SE Tibet, China: petrological and geochemical constraints on petrogenesis. J. Petrol. 46, 33–78.
Hart, S.R., Gerlach, D.C., White, W.M., 1986. A possible new Sr-Nd-Pb mantle array and consequences for mantle mixing. Geochim. Cosmochim. Acta 50, 1551–1557.
Hart, S.R., 1984. A large-scale isotope anomaly in the Southern Hemisphere mantle. Nature 309, 753–757.
He, S.P., Li, R.S., Wang, C., Zhang, H.F., Ji, W.H., Yu, P.S., Gu, P.Y., Shi, C., He, S.P., Li, R.S., 2011. Discovery of ~4.0 Ga detrital zircons in the Changdu Block, North Qiangtang, Tibetan Plateau. Sci. Bull. 56, 647–658.
Hellebrand, E., Snow, J.E., Hoppe, P., Hofmann, A.W., 2002. Garnet-field melting and late-stage refertilization in ‘residual’abyssal peridotites from the Central Indian Ridge. J. Petrol. 43, 2305–2338.
Horton, B.K., Yin, A., Spurlin, M.S., Zhou, J., Wang, J., 2002. Paleocene-Eocene syncontractional sedimentation in narrow, lacustrine-dominated basins of east-central Tibet. Geol. Soc. Am. Bull. 114, 771–786.
Hou, Z., Zaw, K., Pan, G., Mo, X., Xu, Q., Hu, Y., Li, X., 2007. Sanjiang Tethyan metallogenesis in SW China: tectonic setting, metallogenic epochs and deposit types. Ore Geol. Rev. 31, 48–87.
Hou, Z., Hongwen, M., Zaw, K., Yuquan, Z., Mingjie, W., Zeng, W., Guitang, P., Renli, T., 2003. The Himalayan Yulong porphyry copper belt: Product of large-scale strike-slip faulting in eastern Tibet. Econ. Geol. 98, 125–145.
Hu, X., Garzanti, E., Wang, J., Huang, W., An, W., Webb, A., 2016. The timing of India-Asia collision onset – facts, theories, controversies. Earth Sci. Rev. 160, 264–299.
Hu, X., Wang, J., An, W., Garzanti, E., Li, J., 2017. Constraining the timing of the India-Asia continental collision by the sedimentary record. Sci. China Earth Sci. 60,

603–625.
Huang, X.-L., Niu, Y., Xu, Y.-G., Chen, L.-L., Yang, Q.-J., 2010. Mineralogical and geochemical constraints on the petrogenesis of post-collisional potassic and ultrapotassic rocks from western Yunnan, SW China. J. Petrol. 51, 1617–1654.
Irvine, T., Baragar, W., 1971. A guide to the chemical classification of the common volcanic rocks. Can. J. Earth Sci. 8, 523–548.
Irving, A.J., Frey, F.A., 1984. Trace element abundances in megacrysts and their host basalts: constraints on partition coefficients and megacryst genesis. Geochimica et Cosmochimica Acta 48, 1201–1221.
Jacobsen, S.B., Wasserburg, G., 1980. Sm-Nd isotopic evolution of chondrites. Earth Planet. Sci. Lett. 50, 139–155.
Jian, P., Liu, D., Kröner, A., Zhang, Q., Wang, Y., Sun, X., Zhang, W., 2009. Devonian to Permian plate tectonic cycle of the Paleo-Tethys Orogen in southwest China (II): insights from zircon ages of ophiolites, arc/back-arc assemblages and within-plate igneous rocks and generation of the Emeishan CFB province. Lithos 113, 767–784.
Jiang, Y.-H., Jiang, S.-Y., Ling, H.-F., Dai, B.-Z., 2006. Low-degree melting of a metasomatized lithospheric mantle for the origin of Cenozoic Yulong monzogranite-porphyry, east Tibet: geochemical and Sr-Nd-Pb-Hf isotopic constraints. Earth Planet. Sci. Lett. 241, 617–633.
Le Bas, M., Le Maitre, R., Streckeisen, A., Zanettin, B., 1986. A chemical classification of volcanic rocks based on the total alkali-silica diagram. J. Petrol. 27, 745–750.
Le Maitre, R.W., Bateman, P., Dudek, A., Keller, J., Lameyre, J., Le Bas, M., Sabine, P., Schmid, R., Sorensen, H., Streckeisen, A., 1989. A classification of igneous rocks and glossary of terms: Recommendations of the International Union of Geological Sciences Subcommission on the Systematics of Igneous Rocks. Blackwell Oxford.
Li, Z.-X., Li, X., Kinny, P., Wang, J., Zhang, S., Zhou, H., 2003. Geochronology of Neoproterozoic syn-rift magmatism in the Yangtze Craton, South China and correlations with other continents: evidence for a mantle superplume that broke up Rodinia. Precambr. Res. 122, 85–109.
Liu, D., Zhao, Z., Depaolo, D.J., Zhu, D.C., Meng, F.Y., Shi, Q., Wang, Q., 2016. Potassic volcanic rocks and adakitic intrusions in southern Tibet: Insights into mantle-crust interaction and mass transfer from Indian plate. Lithos 268–271, 48–64.
Liu, D., Zhao, Z., Zhu, D.-C., Niu, Y., Widom, E., Teng, F.-Z., DePaolo, D.J., Ke, S., Xu, J.-F., Wang, Q., 2015. Identifying mantle carbonatite metasomatism through Os-Sr-Mg isotopes in Tibetan ultrapotassic rocks. Earth Planet. Sci. Lett. 430, 458–469.
Liu, P.P., Zhou, M.F., Zhao, G.C., Chung, S.L., Chen, W.T., Wang, F., 2017. Eocene granulite-facies metamorphism prior to deformation of the Mianhuadi mafic complex in the Ailao Shan-Red River shear zone, Yunnan province SW China. J. Asian Earth Sci. 145, 626–640.
Liu, Y., Gao, S., Hu, Z., Gao, C., Zong, K., Wang, D., 2010. Continental and Oceanic Crust Recycling-induced MeltPeridotite Interactions in the Trans-North China Orogen: U-Pb Dating, Hf Isotopes and Trace Elements in Zircons from Mantle Xenoliths. J. Petrol. 51, 392–399.
Liu, Y., Hu, Z., Gao, S., Günther, D., Xu, J., Gao, C., Chen, H., 2008. In-situ analysis of major and trace elements of anhydrous minerals by LA-ICP-MS without applying an internal standard. Chem. Geol. 257, 34–43.
Liu, Z.-Q., Li, X.-Z., Ye, Q.-T., Luo, J.-N., Shen, G.-F., 1993. Division of tectono-magmatic belts and the distribution of deposits in the Sanjiang area. Geological Publishing House, Beijing, pp. 246 (in Chinese with English abstract).
Lu, Y.-J., McCuaig, T.C., Li, Z.-X., Jourdan, F., Hart, C.J., Hou, Z.-Q., Tang, S.-H., 2015. Paleogene post-collisional lamprophyres in western Yunnan, western Yangtze Craton: Mantle source and tectonic implications. Lithos 233, 139–161.
Lu, Y.-J., Kerrich, R., Kemp, A.I., McCuaig, T.C., Hou, Z.-Q., Hart, C.J., Li, Z.-X., Cawood, P.A., Bagas, L., Yang, Z.-M., 2013a. Intracontinental eocene-oligocene porphyry Cu mineral systems of Yunnan, Western Yangtze Craton, China: compositional characteristics, sources, and implications for continental collision metallogeny. Econ. Geol. 108, 1541–1576.
Lu, Y.-J., Kerrich, R., Mccuaig, T.C., Li, Z.-X., Hart, C.J., Cawood, P.A., Hou, Z.-Q., Bagas, L., Cliff, J., Belousova, E.A., 2013b. Geochemical, Sr-Nd-Pb, and zircon Hf-O isotopic compositions of Eocene-Oligocene shoshonitic and potassic adakite-like felsic intrusions in western Yunnan, SW China: petrogenesis and tectonic implications. J. Petrol. 54, 1309–1348.
Lu, Y.-J., Kerrich, R., Cawood, P.A., McCuaig, T.C., Hart, C.J., Li, Z.-X., Hou, Z.-Q., Bagas, L., 2012. Zircon SHRIMP U-Pb geochronology of potassic felsic intrusions in western Yunnan, SW China: constraints on the relationship of magmatism to the Jinsha suture. Gondwana Res. 22, 737–747.
Lugmair, G., Marti, K., 1978. Lunar initial $^{143}Nd/^{144}Nd$: differential evolution of the lunar crust and mantle. Earth Planet. Sci. Lett. 39, 349–357.
Ludwig, K., 2012. A Geochronological Toolkit for Microsoft Excel. Berkeley Geochronology Center Special Publications 1–75.
McCulloch, M., Black, L., 1984. Sm Nd isotopic systematics of Enderby Land granulites and evidence for the redistribution of Sm and Nd during metamorphism. Earth Planet. Sci. Lett. 71, 46–58.
McKenzie, D., O'nions, R., 1991. Partial melt distributions from inversion of rare earth element concentrations. J. Petrol. 32, 1021–1091.
Metcalfe, I., 2013. Gondwana dispersion and Asian accretion: tectonic and palaeogeographic evolution of eastern Tethys. J. Asian Earth Sci. 66, 1–33.
Miller, C., Schuster, R., Klötzli, U., Frank, W., Purtscheller, F., 1999. Post-collisional potassic and ultrapotassic magmatism in SW Tibet: geochemical and Sr-Nd-Pb-O isotopic constraints for mantle source characteristics and petrogenesis. J. Petrol. 40, 1399–1424.
Mo, X., Zhao, Z., Deng, J., Flower, M., Yu, X., Luo, Z., Li, Y., Zhou, S., Dong, G., Zhu, D., 2006. Petrology and geochemistry of postcollisional volcanic rocks from the Tibetan plateau: implications for lithosphere heterogeneity and collision-induced asthenospheric mantle flow. Geol. Soc. Am. Spec. Pap. 409, 507–530.
Mo, X., Lu, F., Shen, S., Zhu, Q., Hou, Z., 1993. The Tethyan volcanism and mineralization in the Sanjiang region. Beijing, Geological Publishing House, p. 250 (in Chinese with English abstract).
Nowell, G., Pearson, D., Bell, D., Carlson, R., Smith, C., Kempton, P., Noble, S., 2004. Hf isotope systematics of kimberlites and their megacrysts: new constraints on their source regions. J. Petrol. 45, 1583–1612.
Nowell, G., Kempton, P., Noble, S., Fitton, J., Saunders, A., Mahoney, J., Taylor, R., 1998. High precision Hf isotope measurements of MORB and OIB by thermal ionisation mass spectrometry: insights into the depleted mantle. Chem. Geol. 149, 211–233.
Pan, G., 1990. Tectonic Evolution of the Qinhai-Tibet Plateau. Geological Publishiing House, Beijing, pp. 345–346.
Pang, K.-N., Chung, S.-L., Zarrinkoub, M.H., Wang, F., Kamenetsky, V.S., Lee, H.-Y., 2015. Quaternary high-Mg ultrapotassic rocks from the Qal'eh Hasan Ali maars, southeastern Iran: petrogenesis and geodynamic implications. Contrib. Miner. Petrol. 170, 1–19.
Peucat, J., Vidal, P., Bernard-Griffiths, J., Condie, K., 1989. Sr, Nd, and Pb isotopic systematics in the archean low-to high-grade transition zone of Southern India: syn-accretion vs. post-accretion granulites. J. Geol. 537–549.
Plank, T., Langmuir, C.H., 1998. The chemical composition of subducting sediment and its consequences for the crust and mantle. Chem. Geol. 145, 325–394.
Polat, A., Münker, C., 2004. Hf-Nd isotope evidence for contemporaneous subduction processes in the source of late Archean arc lavas from the Superior Province, Canada. Chem. Geol. 213, 403–429.
Prelević, D., Akal, C., Foley, S.F., Romer, R.L., Stracke, A., Bogaard, P.V.D., 2012. Ultrapotassic mafic rocks as geochemical proxies for post-collisional dynamics of orogenic lithospheric mantle: the case of southwestern Anatolia, Turkey. J. Petrol. 53, 1019–1055.
Prelević, D., Foley, S.F., Romer, R., Conticelli, S., 2008. Mediterranean Tertiary lamproites derived from multiple source components in postcollisional geodynamics. Geochim. Cosmochim. Acta 72, 2125–2156.
Pullen, A., Kapp, P., Gehrels, G.E., Vervoort, J.D., Ding, L., 2008. Triassic continental subduction in central Tibet and Mediterranean-style closure of the Paleo-Tethys Ocean. Geology 36, 351–354.
Qi, L., Jing, H., Gregoire, D.C., 2000. Determination of trace elements in granites by inductively coupled plasma mass spectrometry. Talanta 51, 507–513.
Richard, P., Shimizu, N., Allegre, C., 1976. $^{143}Nd/^{146}Nd$, a natural tracer: an application to oceanic basalts. Earth Planet. Sci. Lett. 31, 269–278.
Smith, R.E., Smith, S.E., 1976. Comments on the use of Ti, Zr, Y, Sr, K, P and Nb in classification of basaltic magmas. Earth Planet. Sci. Lett. 32, 114–120.
Roger, F., Tapponnier, P., Arnaud, N., SchaÈrer, U., Brunel, M., Zhiqin, X., Jingsui, Y., 2000. An Eocene magmatic belt across central Tibet: mantle subduction triggered by the Indian collision? Terra Nova 12, 102–108.
Roger, F., Calassou, S., 1997. U-Pb geochronology on zircon and isotope geochemistry (Pb, Sr and Nd) of the basement in the Songpan-Garze fold belt (China). Comptes Rendus de l'Academie des Sciences Series IIA Earth and Planetary Science 10, 819–826.
Rudnick, R.L., Fountain, D.M., 1995. Nature and composition of the continental crust: a lower crustal perspective. Rev. Geophys. 33, 267–309.
Scherer, E., Münker, C., Mezger, K., 2001. Calibration of the lutetium-hafnium clock. Science 293, 683–687.
Sun, H., Deng, W., Zhang, Y., 2001. Petrogenesis of Cenozoic potassic volcanic rocks in the Nangqen basin. Acta Geol. Sin. 75, 27–40 (in Chinese with English abstract).
She, Z., Ma, C., Mason, R., Li, J., Wang, G., Lei, Y., 2006. Provenance of the Triassic Songpan-Ganzi flysch, west China. Chem. Geol. 231, 159–175.
Song, X.-Y., Zhou, M.-F., Cao, Z.-M., Robinson, P.T., 2004. Late Permian rifting of the South China Craton caused by the Emeishan mantle plume? J. Geol. Soc. 161, 773–781.
Spurlin, M.S., Yin, A., Horton, B.K., Zhou, J., Wang, J., 2005. Structural evolution of the Yushu-Nangqian region and its relationship to syncollisional igneous activity, east-central Tibet. Geol. Soc. Am. Bull. 117, 1293–1317.
Steiger, R.H., Jäger, E., 1977. Subcommission on geochronology: convention on the use of decay constants in geo-and cosmochronology. Earth Planet. Sci. Lett. 36, 359–362.
Sun, S.-S., McDonough, W.F., 1989. Chemical and isotopic systematics of oceanic basalts: implications for mantle composition and processes. Geol. Soc. Lond. Spec. Publications 42, 313–345.
Sun, W.-H., Zhou, M.-F., Gao, J.-F., Yang, Y.-H., Zhao, X.-F., Zhao, J.-H., 2009. Detrital zircon U-Pb geochronological and Lu-Hf isotopic constraints on the Precambrian magmatic and crustal evolution of the western Yangtze Block, SW China. Precambr. Res. 172, 99–126.
Sun, X., Lu, Y.-J., McCuaig, T.C., Zheng, Y.-Y., Chang, H.-F., Guo, F., Xu, L.-J., 2018. Miocene ultrapotassic, high-Mg dioritic, and adakite-like rocks from Zhunuo in Southern Tibet: implications for mantle metasomatism and porphyry copper mineralization in collisional orogens. J. Petrol. 59, 341–386.
Tao, Y., Bi, X., Li, C., Hu, R., Li, Y., Liao, M., 2014. Geochronology, petrogenesis and tectonic significance of the Jitang granitic pluton in eastern Tibet, SW China. Lithos 184–187, 314–323.
Tapponnier, P., Zhiqin, X., Roger, F., Meyer, B., Arnaud, N., Wittlinger, G., Jingsui, Y., 2001. Oblique stepwise rise and growth of the Tibet Plateau. Science 294, 1671–1677.
Taylor, S.R., McLennan, S.M., 1985. The Continental Crust: Its Composition and Evolution. BlackwellScientific Publications, United States, pp. 1–328.
Tera, F., Wasserburg, G., 1972. U-Th-Pb systematics in three Apollo 14 basalts and the problem of initial Pb in lunar rocks. Earth Planet. Sci. Lett. 14, 281–304.
Todt, W., Cliff, R., Hanser, A., Hofmann, A., 1996. Evaluation of a ^{202}Pb-^{205}Pb double spike for high-precision lead isotope analysis. Washington DC American Geophysical Union Geophysical Monograph Series 95, 429–437.
Turner, S., Arnaud, N., Liu, J., Rogers, N., Hawkesworth, C., Harris, N., Kelley, S., Van

Calsteren, P., Deng, W., 1996. Post-collision, shoshonitic volcanism on the Tibetan Plateau: implications for convective thinning of the lithosphere and the source of ocean island basalts. J. Petrol. 37, 45–71.
Usuki, T., Lan, C.Y., Wang, K.L., Chiu, H.Y., 2013. Linking the Indochina block and Gondwana during the Early Paleozoic: evidence from U-Pb ages and Hf isotopes of detrital zircons. Tectonophysics 586, 145–159.
Vervoort, J.D., Patchett, P.J., Blichert-Toft, J., Albarède, F., 1999. Relationships between Lu-Hf and Sm-Nd isotopic systems in the global sedimentary system. Earth Planet. Sci. Lett. 168, 79–99.
Wang, C., Bagas, L., Lu, Y., Santosh, M., Du, B., McCuaig, T.C., 2016. Terrane boundary and spatio-temporal distribution of ore deposits in the Sanjiang Tethyan Orogen: insights from zircon Hf-isotopic mapping. Earth Sci. Rev. 156, 39–65.
Wang, J.-H., Yin, A., Harrison, T.M., Grove, M., Zhang, Y.-Q., Xie, G.-H., 2001. A tectonic model for Cenozoic igneous activities in the eastern Indo-Asian collision zone. Earth Planet. Sci. Lett. 188, 123–133.
Wang, P.-L., Lo, C.-H., Chung, S.-L., Lee, T.-Y., Lan, C.-Y., Van Thang, T., 2000. Onset timing of left-lateral movement along the Ailao Shan-Red River Shear Zone: $^{40}Ar/^{39}Ar$ dating constraint from the Nam Dinh Area, northeastern Vietnam. J. Asian Earth Sci. 18, 281–292.
Wang, Q., Deng, J., Li, C., Li, G., Yu, L., Qiao, L., 2013. The boundary between the Simao and Yangtze blocks and their locations in Gondwana and Rodinia: constraints from detrital and inherited zircons. Gondwana Res. 26, 438–448.
Wang, Q., Wyman, D.A., Li, Z.-X., Sun, W., Chung, S.-L., Vasconcelos, P.M., Zhang, Q., Dong, H., Yu, Y., Pearson, N., 2010. Eocene north-south trending dikes in central Tibet: new constraints on the timing of east-west extension with implications for early plateau uplift? Earth Planet. Sci. Lett. 298, 205–216.
Wang, Q., Wyman, D.A., Xu, J., Dong, Y., Vasconcelos, P.M., Pearson, N., Wan, Y., Dong, H., Li, C., Yu, Y., 2008. Eocene melting of subducting continental crust and early uplifting of central Tibet: evidence from central-western Qiangtang high-K calc-alkaline andesites, dacites and rhyolites. Earth Planet. Sci. Lett. 272, 158–171.
Wang, Q., Xu, J.-F., Jian, P., Bao, Z.-W., Zhao, Z.-H., Li, C.-F., Xiong, X.-L., Ma, J.-L., 2006. Petrogenesis of adakitic porphyries in an extensional tectonic setting, Dexing, South China: implications for the genesis of porphyry copper mineralization. J. Petrol. 47, 119–144.
Wang, R., Weinberg, R.F., Collins, W.J., Richards, J.P., Zhu, D.C., 2018a. Origin of postcollisional magmas and formation of porphyry Cu deposits in southern Tibet. Earth Sci. Rev. 181, 122–143.
Wang, R., Richards, J.P., Zhou, L.-M., Hou, Z.-Q., Stern, R.A., Creaser, R.A., Zhu, J.-J., 2015. The role of Indian and Tibetan lithosphere in spatial distribution of Cenozoic magmatism and porphyry Cu-Mo deposits in the Gangdese belt, southern Tibet. Earth Sci. Rev. 150, 68–94.
Wang, Y., Qian, X., Cawood, P.A., Liu, H., Feng, Q., Zhao, G., Zhang, Y., He, H., Zhang, P., 2018b. Closure of the East Paleotethyan Ocean and amalgamation of the Eastern Cimmerian and Southeast Asia continental fragments. Earth Sci. Rev. 186, 195–230.
Wu, F.Y., Ji, W.Q., Wang, J.G., Liu, C.Z., Chung, S.L., Clift, P.D., 2014. Zircon U-Pb and Hf isotopic constraints on the onset time of India-Asia collision. Am. J. Sci. 314, 548–579.
Wu, F.-Y., Yang, Y.-H., Xie, L.-W., Yang, J.-H., Xu, P., 2006. Hf isotopic compositions of the standard zircons and baddeleyites used in U-Pb geochronology. Chem. Geol. 234, 105–126.
Xia, L., Li, X., Ma, Z., Xu, X., Xia, Z., 2011. Cenozoic volcanism and tectonic evolution of the Tibetan plateau. Gondwana Res. 19, 850–866.
Xu, B., Griffin, W.L., Xiong, Q., Hou, Z.Q., O'Reilly, S.Y., Guo, Z., Pearson, N.J., Gréau, Y., Yang, Z.M., Zheng, Y.C., 2017. Ultrapotassic rocks and xenoliths from South Tibet: contrasting styles of interaction between lithospheric mantle and asthenosphere during continental collision. Geology 45, 51–54.
Xu, L., Bi, X., Hu, R., Zhang, X., Su, W., Qu, W., Hu, Z., Tang, Y., 2012. Relationships between porphyry Cu-Mo mineralization in the Jinshajiang-Red River metallogenic belt and tectonic activity: constraints from zircon U-Pb and molybdenite Re-Os geochronology. Ore Geol. Rev. 48, 460–473.
Xu, Y.-G., Menzies, M.A., Thirlwall, M.F., Xie, G.-H., 2001. Exotic lithosphere mantle beneath the western Yangtze craton: petrogenetic links to Tibet using highly magnesian ultrapotassic rocks. Geology 29, 863–866.
Xu, Y., Bi, X.W., Hu, R.Z., Chen, Y.W., Liu, H.Q., Xu, L.L., 2016. Geochronology and geochemistry of Eocene potassic felsic intrusions in the Nangqian basin, eastern Tibet: tectonic and metallogenic implications. Lithos 246–247, 212–227.
Yang, T.J., Sun, X.M., Shi, G.Y., Lu, Y., Fu, Y., 2019a. Constraints on the left lateral shearing and crustal melting of the Ailaoshan Massif, Yunnan Province, Southwest China. J. Asian Earth Sci. 177, 186–197.
Yang, T.J., Sun, X.M., Shi, G.Y., Li, D.S., Zhou, H.Y., 2019b. The genetic linkage between the Yuanjiang marble-hosted ruby deposit and Cenozoic tectonic evolution of the Ailao Shan-Red River shear zone (Southwest China). J. Asian Earth Sci. 177, 38–47.
Yang, Z.M., Lu, Y.J., Hou, Z.Q., Chang, Z.S., 2015. High-Mg Diorite from Qulong in Southern Tibet: implications for the Genesis of Adakite-like Intrusions and Associated Porphyry Cu Deposits in Collisional Orogens. J. Petrol. 56, 227–254.
Zhang, H.-F., Sun, M., Zhou, X.-H., Fan, W.-M., Zhai, M.-G., Yin, J.-F., 2002. Mesozoic lithosphere destruction beneath the North China Craton: evidence from major-, trace-element and Sr-Nd-Pb isotope studies of Fangcheng basalts. Contrib. Miner. Petrol. 144, 241–254.
Zhang, H., He, H., Wang, J., Xie, G., 2005. $^{40}Ar/^{39}Ar$ chronology and geochemistry of high-K volcanic rocks in the Mangkang basin. Tibet. Sci. China Series D: Earth Sci. 48, 1–12.
Zhang, Y., Xie, Y., 1997. Geochronology of Ailaoshan-Jinshajiang alkalirich intrusive rocks and their Sr and Nd isotopic characteristics. Sci. China, Ser. D Earth Sci. 40, 524–529.
Zhang, Y.C., Shi, G.R., Shen, S.Z., 2013. A review of Permian stratigraphy, palaeobiogeography and palaeogeography of the Qinghai-Tibet Plateau. Gondwana Res. 24, 55–76.
Zhao, Z., Mo, X., Dilek, Y., Niu, Y., DePaolo, D.J., Robinson, P., Zhu, D., Sun, C., Dong, G., Zhou, S., 2009. Geochemical and Sr-Nd-Pb-O isotopic compositions of the post-collisional ultrapotassic magmatism in SW Tibet: petrogenesis and implications for India intra-continental subduction beneath southern Tibet. Lithos 113, 190–212.
Zheng, Y., Wu, F., 2018. The timing of continental collision between Indian and Asia. Sci. Bull. 63, 1649–1654.
Zhou, M.-F., Zhao, X.-F., Chen, W.T., Li, X.-C., Wang, W., Yan, D.-P., Qiu, H.-N., 2014. Proterozoic Fe–Cu metallogeny and supercontinental cycles of the southwestern Yangtze Block, southern China and northern Vietnam. Earth Sci. Rev. 139, 59–82.
Zhou, M.-F., Ma, Y., Yan, D.-P., Xia, X., Zhao, J.-H., Sun, M., 2006. The Yanbian terrane (Southern Sichuan Province, SW China): a Neoproterozoic arc assemblage in the western margin of the Yangtze block. Precambr. Res. 144, 19–38.
Zhu, D.C., Wang, Q., Zhao, Z.D., 2017. Constraining quantitatively the timing and process of continent-continent collision using magmatic record: method and examples. Sci. China Earth Sci. 60, 1040–1056.
Zhu, D.C., Zhao, Z.D., Niu, Y., Dilek, Y., Hou, Z.Q., Mo, X.X., 2013. The origin and pre-Cenozoic evolution of the Tibetan Plateau. Gondwana Res. 23, 1429–1454.
Zi, J.-W., Cawood, P.A., Fan, W.-M., Tohver, E., Wang, Y.-J., Mccuaig, T.C., Peng, T.-P., 2013. Late Permian-Triassic magmatic evolution in the Jinshajiang orogenic belt, SW China and implications for orogenic processes following closure of the Paleo-Tethys. Am. J. Sci. 313, 81–112.
Zi, J.-W., Cawood, P.A., Fan, W.-M., Tohver, E., Wang, Y.-J., McCuaig, T.C., 2012. Generation of Early Indosinian enriched mantle-derived granitoid pluton in the Sanjiang Orogen (SW China) in response to closure of the Paleo-Tethys. Lithos 140, 166–182.
Zindler, A., Hart, S., 1986. Chemical geodynamics. Annu. Rev. Earth Planet. Sci. 14, 493–571.